THEORETICAL STUDY OF ELECTRONIC PROPERTIES OF THE CU(001) SURFACE UNDER CONDITIONS OF HIGH COVERAGE OXIDATION

by

WILLIE BURTON MADDOX IV

Presented to the Faculty of the Graduate School of
The University of Texas at Arlington in Partial Fulfillment
of the Requirements
for the Degree of

MASTER OF SCIENCE IN PHYSICS

THE UNIVERSITY OF TEXAS AT ARLINGTON

May 2009

To my family...

ACKNOWLEDGEMENTS

I would first like to thank my thesis advisors. My supervising professor, Dr. Nail Fazleev, constantly motivating and encouraging me, and also for his invaluable knowledge especially concerning electronic structure theory. Dr. Alex Weiss not only helped me gain an understanding of experimental positron techniques, but also ultra high vacuum system operation. I would like to thank Dr. John Fry who provided useful comments as well, especially on the topic of band structure. I would also like to thank Dr. Asok Ray and his group, specifically Dr. Pratik Dholabhai and Dr. Raymond Atta-Fynn for their valuable comments on density functional theory and the operation of the DMol3 code. Also from UTA I would like to thank Amy Osborn and Margie Jackymack for their invaluable administrative services. From outside UTA I wish to express my deepest gratitude to Dr. Juarez Da Silva for his comments on density plotting and also Dr. Aloysius Soon for his comments regarding Copper Oxide. I would also like to thank Dr. Alex Goldberg and Dr. Jian-Jie Liang of Accelrys who offered helpful tips with DMol3 and Materials Studio.

I am grateful to all the teachers who educated me during the years I spent in school. From Madison Academy I wish to thank Mary Chunn, Bob Trammel, Darla Blackburn, and Denise Parrish. From the University of Alabama in Huntsville I would like to thank Dr. Carol Strong, Dr. Rich Miller, Dr. James Miller, and particularly Dr. Ted Rogers who convinced me to pursue a life in the physical sciences. I would also like to thank Vanessa DeWitt and Brett MacWilliams for their useful comments. I wish to thank all the staff in the Space Plasma Physics Group at the National Space Science and Technology Center in Huntsville Alabama. I wish to extend special

thanks to Dr. Paul Craven, Dr. James Spann, and Dr. Glynn Germany who taught me excellent techniques in imaging, data analysis and project presentation.

Finally, I would like to express my deepest gratitude to my mother, father, and sister who have encouraged and inspired me and sponsored my undergraduate and graduate studies. I am extremely fortunate to be so blessed. I am also extremely grateful for their sacrifice, encouragement and patience. I also wish to thank all of my friends who have helped me throughout my career.

May 4, 2009

ABSTRACT

THEORETICAL STUDY OF ELECTRONIC PROPERTIES
OF THE CU(001) SURFACE UNDER CONDITIONS
OF HIGH COVERAGE OXIDATION

WILLIE BURTON MADDOX IV, M.S.
The University of Texas at Arlington, 2009

Supervising Professor: NAIL FAZLEEV

The study of adsorption of oxygen on transition metal surface is important for the understanding of oxidation, heterogeneous catalysis, and metal corrosion. The structures formed on oxidized transition metal surfaces vary from simple adlayers of chemisorbed oxygen to more complex structures which result from the diffusion of oxygen into sub-surface regions. In this thesis, an *ab-initio* investigation of stability and associated physical and electronic properties of different adsorption phases of oxygen on Cu(001) as well as of the clean copper surfaces using density functional theory in the generalized gradient approximation, is presented. All surface geometries are fully optimized. Results of calculation include the changes in electron work function, interlayer spacing, difference electron density and density of states as a function of oxygen coverage. Furthermore, the chemistry of metal-adsorbate bonding is studied with primary interest being paid to high coverage oxygen adsorption.

TABLE OF CONTENTS

LIST OF FIGURES

LIST OF TABLES

ACRONYMS

ASA	Atomic Spheres Approximation
ARUPS	Angle-Resolved Ultraviolet Photoemission Spectroscopy
BOA	Born-Oppenheimer Approximation
DFT	Density Functional Theory
FP-LAPW	Full Potential Linearized Augmented Plane Wave
FP-LMTO	Full Potential Linearized Muffin Tin Orbital
GGA	Generalized Gradient Approximation
HK	Hohenberg-Kohn
LCAO	Linear Combination of Atomic Orbitals
LDA	Local Density Approximation
LEED	Low Energy Electron Diffraction
MAPW	Modified Augmented Plane Wave
PBE	Perdew Burke Ernzerhof
PDOS	Partial Density of States
PE	Photoelectric Effect
PPPW	Pseudopotential Plane Waves
SCF	Self-Consistent Field
SLEEP	Scanning Low Energy Electron Probe
SUC	Surface Unit Cell
UPS	Ultraviolet Photoemission Spectroscopy
TB-LMTO	Tight Binding Linearized Muffin Tin Orbital
XPS	X-ray Photoemission Spectroscopy

CHAPTER 1

INTRODUCTION

The study of surfaces is one of the most widely studied areas in condensed matter physics and materials science. Nearly everything we interact with involves a surface of some kind. A surface can be characterized as the place where the molecules of a liquid or gas come in contact with the material. The process by which molecules or atoms of a gas accumulate on the surface of a solid to form a thin film is known as Adsorption.[1] Depending on the surface material or substrate, the approaching atoms may form new bonds with the surface. In the case of a copper, the most common adsorption process involves oxidation which occurs naturally under normal atmospheric conditions [1]. This process, known as corrosion, is usually a harmful process. Much effort has been put into the development of materials to resist corrosion. Alloys such as stainless steel are good examples of this.

In order for a material to be resistant to corrosion, the surface should be repulsive toward gas phase oxygen. For many metals, like aluminum, this is achieved by forming a thin oxide film on the metal surface thereby creating a protective barrier over the substrate which prevents further corrosion. In addition, these oxide films are currently used in metal to metal adhesion [2, 3], the sealing of electronic packaging [4, 5], and various biomedical applications [6–8].

In some cases the oxides that form on metals can have better catalytic properties than the metals themselves [9]. For example, copper based catalysts are known to react well in the partial oxidation and synthesis of methanol and the extraction

[1] Not to be confused with absorption which is a process in which one substance permeates another.

of hydrogen from water which are important stages in the water gas shift [10, 11]. Copper oxides are also used in other areas of renewable energy research. One of the most attractive qualities of copper oxides is their aptness to be good renewable energy materials. The copper oxide known as cuprite, or Cu_2O, is a p-type semiconductor with a 2eV band gap which makes it a good candidate for use in solar cell materials [12]. In addition, recent studies have shown that the copper oxide, CuO, could be a possible candidate in photoelectrochemical water splitting [13–17].

Pure copper also has its own advantages. The electrical and thermal conductivity of copper is higher than it is for all other elements in the periodic table except silver. In comparison to other transition metals copper is abundant and has a relatively low cost. In industrial applications, copper has been predominantly the main material used in electrical wiring over the past several years. It has also proven to be a usable interconnecting material in microprocessors [18]. Another advantage of copper is that it oxidizes quite easily. However, because the oxidation process occurs so rapidly, it makes it difficult to control the adsorption and reactivity of the adsorbates on the surface.

Based on these facts, it is easy to see the importance in gaining further understanding concerning the surface properties of metals and oxides that form on them. A vast amount of research both experimental and theoretical has been done already to look at various properties of copper and copper oxides [19–32]. This is beneficial because not only does it serve as a benchmark for comparing results obtained from new techniques, but it also allows us to build upon the current methods by exploring even larger more complex systems. Despite the numerous experimental and theoretical studies there are still many surface properties of metal oxides are not well understood such as diffusion of oxygen into sub-surface regions and the reconstructions that take place at high coverages. This thesis focuses on both of these.

In Chapter 2 the general theory behind all calculations performed in this thesis is discussed. In Chapter 3 an overview of surface structure will be presented which will provide an analysis of the results pertaining to low index clean copper surfaces. In Chapter 4 low coverage ($0.0 \leq \Theta \leq 0.5$ ML) oxygen adsorption specifically on the Cu(001) surface will be covered. In Chapter 5, results and discussion of highly oxidized copper surfaces will be presented. Conclusions are given in Chapter 6.

CHAPTER 2

THEORETICAL APPROACH

This chapter is divided into five parts. Section 2.1, will give a brief introduction followed by a discussion of many-body theory in section 2.2. Section 2.3 summarizes the Born-Oppenheimer approximation. Section 2.4 surveys the key elements of Density Functional Theory (DFT) with a comprehensive flow chart diagram explanation of the DMol3 computer code in 2.5.

2.1 Introduction

The aim of first principles calculations is to predict the physical properties of materials systems excluding input from experimental data. Using information based solely on the constituent atoms, all physical characteristics should be determined quantum-mechanically without the need for oversimplifications or approximations. Currently, there is no solution to the many body problem which can be solved exactly by analytical means. Density functional theory offers a solution to such ambitious studies by demonstrating formally how all features of many-electron systems can be derived from the ground-state electronic density alone. This chapter focuses on key aspects of density functional theory as it pertains to the present study and how it is implemented computationally to gain information about these many body systems.

2.2 The Many-Body Problem

All matter is made up of a collection of interacting atoms in a solid, liquid, or gas phase. We can describe all these systems as a set of atomic nuclei and elec-

trons interacting via Coulombic forces. In order to explore the microscopic nature of electronic properties of the system, it is necessary to impose quantum mechanics and solve the time-independent Schrödinger equation,

$$\hat{H}\Psi_n = E_n\Psi_n, \tag{2.1}$$

or in Dirac notation,

$$E_n = \langle\Psi_n|\hat{H}|\Psi_n\rangle, \tag{2.2}$$

where $\hat{H}$ signifies the Hamiltonian operator describing the total energy of the system and E_n is the total energy in the nth state associated with the many-body wave function, Ψ_n.[1] In the many-body system there are N electrons represented by the set of position vectors $\{\mathbf{r}_i\} = \mathbf{r}_1, \mathbf{r}_2, \ldots, \mathbf{r}_N$ and P nuclei represented by $\{\mathbf{R}_I\} = \mathbf{R}_1, \mathbf{R}_2, \ldots, \mathbf{R}_P$.[2] Prior to solving any quantum mechanical problem one must construct the Hamiltonian of the system which includes all kinetic and/or potential energy terms describing the system. For the many-body system containing electrons and nuclei, the general formulation of the Hamiltonian is,

$$\hat{H} = \hat{T}_{nuc} + \hat{T}_{el} + \hat{V}_{nuc-nuc} + \hat{V}_{el-el} + \hat{V}_{el-nuc}. \tag{2.3}$$

The first two terms, $\hat{T}_{nuc}$ and $\hat{T}_{el}$ represent the kinetic energy of the system due to all nuclei and electrons, respectively. The last three terms, $\hat{V}_{nuc-nuc}$, $\hat{V}_{el-el}$, and $\hat{V}_{el-nuc}$ represent the potentials due to nuclear-nuclear, electron-electron, and electron-nuclear interactions, respectively. The first two terms are expressed as,

$$\hat{T}_{nuc} = -\sum_{I=1}^{P} \frac{\hbar^2}{2M_I}\nabla_I^2, \tag{2.4}$$

and,

$$\hat{T}_{el} = -\sum_{i=1}^{N} \frac{\hbar^2}{2m_e}\nabla_i^2, \tag{2.5}$$

[1] All operators in this thesis will be denoted with accents or "hats", (e.g., $\hat{O}$).

[2] Gaussian system of units are used here and throughout the rest of this thesis. $\frac{1}{4\pi\varepsilon_0} = 1$

where $\hbar$ is Planck's constant, the Laplacian operator ∇_I^2 involves differentiation with respect to the position $\mathbf{R}_I$ of the Ith nucleus, and ∇_i^2 involves differentiation with respect to the position $\mathbf{r}_i$ of the ith electron. M_I is the mass of ion I and m_e is the electron mass. The third term, $\hat{V}_{nuc-nuc}$, the Coulomb repulsion between all nuclei, is represented as,

$$\hat{V}_{nuc-nuc} = \frac{1}{2} \sum_{\substack{I=1 \\ I \neq J}}^{P} \sum_{J=1}^{P} \frac{Z_I Z_J e^2}{|\mathbf{R}_I - \mathbf{R}_J|}, \tag{2.6}$$

where the constant e represents the charge of an electron and the variables Z_I and Z_J represent the atomic numbers for nuclei I and J at site $\mathbf{R}_I$ and $\mathbf{R}_J$, respectively. Similarly, $\hat{V}_{el-el}$, the electrostatic repulsion between electrons, is given as,

$$\hat{V}_{el-el} = \frac{1}{2} \sum_{\substack{i=1 \\ i \neq j}}^{N} \sum_{j=1}^{N} \frac{e^2}{|\mathbf{r}_i - \mathbf{r}_j|}. \tag{2.7}$$

The final term in the many-body Hamiltonian, $\hat{V}_{el-nuc}$, represents the electrostatic potential energy between electrons and nuclei in the system,

$$\hat{V}_{el-nuc} = -\sum_{I=1}^{P} \sum_{i=1}^{N} \frac{Z_I e^2}{|\mathbf{R}_I - \mathbf{r}_i|}. \tag{2.8}$$

Note the minus sign in Eq. 2.8 indicates attraction between electrons and nuclei, whereas in Eq. 2.6 and 2.7 the interactions are both repulsive. The value $\frac{1}{2}$ in front of Eq. 2.6 and 2.7 is inserted in order to compensate for double counting of terms in the summations. In practice, this problem is almost impossible to treat within a full quantum mechanical framework due mostly to the multi-component many-body nature that arises when trying to solve Eq. 2.8 and 2.6 exactly. These terms make the Schrödinger equation inseparable.

2.3 The Born-Oppenheimer Approximation

Molecular or atomic motion includes the motion of both nuclei and electrons. The nuclear mass is approximately four orders of magnitude larger than the electron

mass, which leads to the motion of electrons being much faster than that of the nuclei. Therefore, any small movement from the nuclei is quickly compensated for by the electrons, namely the core electrons whose orbitals are closest to the nucleus. Based on this phenomena, the Born-Oppenheimer approximation (BOA) is often implemented which allows us to fix the positions of the nuclei and set $\hat{T}_{nuc}$ equal to zero. Within the BOA, the Hamiltonian of the system takes the form $\hat{H} = \hat{T}_{el} + \hat{V}_{nuc-nuc} + \hat{V}_{el-el} + \hat{V}_{el-nuc}$. In addition, $\hat{V}_{nuc-nuc}$ is simplified to a constant as far as the electron degrees of freedom are concerned, thus we may temporarily exclude it from the Hamiltonian and calculate its value separately. This further reduces the Hamiltonian to,

$$\begin{aligned} \hat{H} &= \hat{T}_{el} + \hat{V}_{el-el} + \hat{V}_{el-nuc} \\ &= -\sum_{i=1}^{N} \frac{\hbar^2}{2m_e} \nabla_i^2 + \frac{e^2}{2} \sum_{\substack{i=1 \\ i \neq j}}^{N} \sum_{j=1}^{N} \frac{1}{|\mathbf{r}_i - \mathbf{r}_j|} - e^2 \sum_{I=1}^{P} \sum_{i=1}^{N} \frac{Z_I}{|\mathbf{R}_I - \mathbf{r}_i|}. \end{aligned} \tag{2.9}$$

Although we have reduced the complexity of the Hamiltonian by imposing the BOA, the task of solving Ψ is still quite difficult.

2.4 Density Functional Theory

One of the most widely used *ab initio* methods for electronic structure calculations in computational condensed matter physics is density functional theory (DFT). The success of DFT is largely attributed to its computational efficiency and its accuracy in numerical calculations. Recall that if there are N electrons in a system, the electron wave function of this system is a function of $3N$ variables. However, in DFT the key variable is the electron density $\rho(\mathbf{r})$, which for a normalized Ψ is given by,

$$\rho(\mathbf{r}) = N \int d\mathbf{r}_2 \int d\mathbf{r}_3 \cdots \int d\mathbf{r}_N \Psi^*(\mathbf{r}, \mathbf{r}_2, \ldots, \mathbf{r}_N) \Psi(\mathbf{r}, \mathbf{r}_2, \ldots, \mathbf{r}_N). \tag{2.10}$$

The importance here lies in the fact that the density has only three degrees of freedom regardless of how large the system is. This is a dramatic simplification of the many-body problem. This idea was first proposed by Thomas and Fermi in the late 1920's based on pure intuition. However, a series of papers in the mid 1960's by Hohenberg, Kohn, and Sham offered the first formal proof of DFT [33, 34].

2.4.1 The Hohenberg-Kohn Theorems

The first Hohenberg-Kohn (HK) theorem states that, besides a trivial additive constant, the external potential is determined uniquely by the ground state electron density. The constant mentioned in the theorem is trivial because any Hamiltonian H will yield the same total energy and wave functions as the Hamiltonian $H + c$, where c is the trivial constant. The constant simply shifts the total energy to a different reference point.

The proof of the first HK theorem is done by *reduction ad absurdum*, or proof by contradiction. The proof is based on the Rayleigh-Ritz variational principle but is otherwise very simple in that the mathematical steps are purely algebraic. To begin, we assume that there exists two *different* potentials $V_{ext}(\mathbf{r})$ and $V'_{ext}(\mathbf{r})$ that each produce the same ground state density $\rho_0(\mathbf{r})$. If these two potentials differ by more than a constant, then they must define two unequal Hamiltonians $\hat{H}$ and $\hat{H}'$. These Hamiltonians would then determine the same ground state density $\rho(\mathbf{r})$ but with different wavefunctions Ψ and Ψ', with $E_0 = \langle\Psi|\hat{H}|\Psi\rangle$ and $E'_0 = \langle\Psi'|\hat{H}'|\Psi'\rangle$. Then by the variational principle,

$$\begin{aligned} E_0 < \langle\Psi'|\hat{H}|\Psi'\rangle &= \langle\Psi'|\hat{H} - \hat{H}' + \hat{H}'|\Psi'\rangle \\ &= \langle\Psi'|\hat{H} - \hat{H}'|\Psi'\rangle + \langle\Psi'|\hat{H}'|\Psi'\rangle \\ &= \int \rho(\mathbf{r})[V_{ext}(\mathbf{r}) - V'_{ext}(\mathbf{r})]d\mathbf{r} + E'_0. \end{aligned} \tag{2.11}$$

Similarly

$$\begin{aligned} E_0' < \langle\Psi|\hat{H}'|\Psi\rangle &= \langle\Psi|\hat{H}' - \hat{H} + \hat{H}|\Psi\rangle \\ &= \langle\Psi|\hat{H}' - \hat{H}|\Psi\rangle + \langle\Psi|\hat{H}|\Psi\rangle \\ &= -\int \rho(\mathbf{r})[V_{ext}(\mathbf{r}) - V_{ext}'(\mathbf{r})]d\mathbf{r} + E_0. \end{aligned} \tag{2.12}$$

When adding Eq. 2.11 and 2.12 together, the integrals cancel and we are left with,

$$E_0 + E_0' < E_0 + E_0', \tag{2.13}$$

which is clearly a contradiction. Hence, the original assumption was incorrect and so there cannot be two different external potentials that give rise to the same ground state density, i.e., $\rho_0(\mathbf{r})$ uniquely determines V_{ext} and vice-versa. The external potential, V_{ext}, may now be used in the Schrödinger equation to generate the ground-state wave function, Ψ. Thus, the ground-state wave function must be a unique functional of the ground-state density,[3]

$$\Psi_0 = \Psi[\rho_0] = \Psi[\rho_0(\mathbf{r})]. \tag{2.14}$$

As a consequence, the expectation value of any observable $\hat{O}$ in the ground-state is also a functional of the ground-state density,

$$O[n_0] = \langle\Psi[\rho_0]|\hat{O}|\Psi[\rho_0]\rangle = \langle\Psi_0|\hat{O}|\Psi_0\rangle. \tag{2.15}$$

Combining Eq. 2.2, 2.9 and 2.15 gives,

$$E_0 = \langle\Psi_0|\hat{H}|\Psi_0\rangle = \langle\Psi_0|\hat{T}_{el} + \hat{V}_{el-el} + \hat{V}_{el-nuc}|\Psi_0\rangle \tag{2.16}$$

$$= \langle\Psi_0|\hat{T}_{el} + \hat{V}_{el-el}|\Psi_0\rangle + \langle\Psi_0|\hat{V}_{el-nuc}|\Psi_0\rangle \tag{2.17}$$

$$E[\rho_0] = F_{HK}[\rho_0] + V_{ext}[\rho_0]. \tag{2.18}$$

[3]A functional is merely a function of some quantity that is a function of some other variable, i.e., a function of a function

The second functional, $V_{ext}[\rho_0]$, is a non-universal functional in that it strictly depends on the system under consideration. Therefore we may write it in terms of the ground-state density $\rho_0(\mathbf{r})$,

$$V_{ext}[\rho_0] = \int V_{ext}(\mathbf{r})\rho_0(\mathbf{r})d\mathbf{r}. \tag{2.19}$$

More generally, the contribution of the external potential can be written explicitly in terms of the density ρ,

$$V_{ext}[\rho] = \int V_{ext}(\mathbf{r})\rho(\mathbf{r})d\mathbf{r}. \tag{2.20}$$

The functional on the right hand side of Eq. 2.16, otherwise known as the HK functional, contains all other functionals that are secondary to $V_{ext}[\rho_0]$. The HK functional is said to be universal because it is valid for any number of particles and for any external potential. We can reformulate the HK functional by decomposing it into smaller parts,

$$F_{HK}[\rho] = T[\rho] + V_H[\rho] + E_{xc}[\rho], \tag{2.21}$$

where $T[\rho]$ represents the kinetic electron energy, and $V_H[\rho]$ and $E_{xc}[\rho]$ represent the Hartree potential energy and the exchange-correlation energy, respectively. The last two terms stem from the electron-electron interaction term and can be grouped together as,

$$\langle\Psi|\hat{V}_{el-el}|\Psi\rangle = V_H[\rho] + E_{xc}[\rho]. \tag{2.22}$$

The reason for grouping the functionals into the HK functional stems from the antisymmetric property of the electron wave function Ψ. In the density functional representation of $\langle\Psi|\hat{V}_{el-el}|\Psi\rangle$ we lose the antisymmetric property of the wave function known as exchange and must therefore describe a new term, E_{xc}, to account for it. Assuming one has got reliable expressions for $T[\rho]$ and $U[\rho]$, we may express the total energy as,

$$E[\rho] = F_{HK}[\rho] + \int V_{ext}(\mathbf{r})\rho(\mathbf{r})d\mathbf{r}. \tag{2.23}$$

A successful minimization of this energy functional will yield the ground-state density ρ_0 and thus all other ground-state observables.

The second HK theorem states that for some trial density $\tilde{\rho}(\mathbf{r}) \geq 0$ which, when integrated, gives the number of electrons as,

$$N = \int \rho_0(\mathbf{r}) d\mathbf{r}, \tag{2.24}$$

we have the following relation,

$$E_0 \leq E[\tilde{\rho}(\mathbf{r})], \tag{2.25}$$

where E_0 is the exact ground state energy and $E[\tilde{\rho}(\mathbf{r})]$ is the energy functional obtained from using the trial density. To prove this, recall from the first HK theorem that $\tilde{\rho}(\mathbf{r})$ determines $\tilde{\Psi}$. Using this as our trial wave function into Eq. 2.16 along with the $V_{ext}(\mathbf{r})$ from the problem of interest gives,

$$\langle \tilde{\Psi} | \hat{H} | \tilde{\Psi} \rangle = F_{HK}[\tilde{\rho}] + \int V_{ext}(\mathbf{r}) \tilde{\rho}(\mathbf{r}) d\mathbf{r} = E[\tilde{\rho}] \geq E[\rho] = E_0, \tag{2.26}$$

where we have again applied the variational principle. This minimizes our total energy. We may now apply the Lagrange method of undetermined multipliers to Eq. 2.25 with Eq. 2.24 as our constraint,

$$\delta \left\{ E[\rho] - \mu \left[\int \rho(\mathbf{r}) d(\mathbf{r}) - N \right] \right\} = 0, \tag{2.27}$$

where μ, the Lagrange multiplier, is actually the chemical potential of the system. Solving Eq. 2.27 for μ we obtain,

$$\mu = \frac{\delta E[\rho]}{\delta \rho(\mathbf{r})} = V_{ext}(\mathbf{r}) + \frac{\delta F_{HK}[\rho(\mathbf{r})]}{\delta \rho(\mathbf{r})}. \tag{2.28}$$

A straightforward application of this formula has two obstacles. First, the exact form of $F_{HK}[\rho]$ is unknown due to the exchange-correlation term. Second, the kinetic term must be formulated in terms of the charge density. Therefore, we must use the set of equations developed by Kohn and Sham to iteratively solve the total energy of the system.

2.4.2 The Kohn-Sham Equations

First assume that the particles are non-interacting. As a result the electron-electron term in the HK functional vanishes and we are left with,

$$F_{HK}[\rho] = T_S[\rho] = -\sum_{i=1}^{N} \langle \psi_i | \frac{\hbar^2}{2m_e} \nabla_r^2 | \psi_i \rangle, \tag{2.29}$$

where the subscript on T_S denotes the use of the Slater determinant [35]. The Schrödinger equation for N non-interacting electrons moving in an external potential, $V_{ext}(\mathbf{r})$, is given as,

$$-\frac{\hbar^2}{2m} \nabla^2 \psi_i(\mathbf{r}) + V_{ext}(\mathbf{r}) \psi_i(\mathbf{r}) = \varepsilon_i \psi_i(\mathbf{r}), \tag{2.30}$$

where ε_i are the ground state energies and the solutions ψ_i may be used to find the charge density,

$$\rho(\mathbf{r}) = \sum_{i=1}^{N} |\psi_i(\mathbf{r})|^2. \tag{2.31}$$

Now for the case of interacting electrons we have,

$$E[\rho] = T_S[\rho] + \int V_{ext}(\mathbf{r}) \rho(\mathbf{r}) d\mathbf{r} + \frac{e^2}{2} \int \frac{\rho(\mathbf{r}) \rho(\mathbf{r}')}{|\mathbf{r} - \mathbf{r}'|} d\mathbf{r} d\mathbf{r}' + E_{xc}[\rho], \tag{2.32}$$

where T_S is the kinetic energy of the non-interacting electrons, V_{ext} is an external potential acting on the system, the third term is the Hartree energy and E_{xc} is the exchange-correlation energy. Taking the differential of Eq. 2.32 gives,

$$\mu = \frac{\delta T_S[\rho]}{\delta \rho(\mathbf{r})} + V_{ext}(\mathbf{r}) + \frac{e^2}{2} \int \frac{\rho(\mathbf{r}')}{|\mathbf{r} - \mathbf{r}'|} d\mathbf{r} d\mathbf{r}' + \frac{\delta E_{xc}[\rho]}{\delta \rho(\mathbf{r})}. \tag{2.33}$$

This equation is similar to Eq. 2.28 but with a more complicated form of the potential,

$$V_{eff}(\mathbf{r}) = V_{ext}(\mathbf{r}) + V_H(\mathbf{r}) + V_{xc}(\mathbf{r}), \tag{2.34}$$

where the Hartree potential is expressed as,

$$V_H(\mathbf{r}) = \frac{e^2}{2} \int \frac{\rho(\mathbf{r}')}{|\mathbf{r} - \mathbf{r}'|} d\mathbf{r}', \tag{2.35}$$

and the exchange-correlation potential is expressed as,

$$V_{xc}(\mathbf{r}) = \frac{\delta E_{xc}[\rho]}{\delta \rho(\mathbf{r})}. \tag{2.36}$$

This leads to the set of Kohn-Sham equations solved from the time independent Schrödinger equation,

$$-\frac{\hbar^2}{2m}\nabla^2\psi_i(\mathbf{r}) + V_{eff}(\mathbf{r})\psi_i(\mathbf{r}) = \varepsilon_i\psi_i(\mathbf{r}). \tag{2.37}$$

The ψ_i's are referred to as Kohn-Sham orbitals and are used to construct a new density of the system. Likewise, the eigenvalues ε_i are used to construct the total energy of the system. Thus, the total energy of the entire system with all energy terms included may be expressed as,

$$E = \sum_i^N \varepsilon_i - \int V_{xc}(r)\rho(\mathbf{r})d\mathbf{r} - \frac{e^2}{2}\int \frac{\rho(\mathbf{r})\rho(\mathbf{r}')}{|\mathbf{r}-\mathbf{r}'|}d\mathbf{r}d\mathbf{r}' + E_{xc}[\rho]. \tag{2.38}$$

Using Eq. 2.31, 2.34, and 2.37 this system must be solved iteratively, until self-consistency is reached. A flow chart for this procedure is provided with discussion in Section 2.5. Up until now, very little has been said about the nature of the exchange-correlation potential, thus it is beneficial to briefly comment on this parameter.

2.4.3 Exchange-Correlation Energy

In principle, the exact total ground state energy of any system can be obtained through DFT. This is true assuming that the exact form of the exchange-correlation functional is known. Unfortunately, no one knows the exact form of the exchange-correlation term. There are however, approximations that exist which allow the calculation of the total energy to great accuracy. The two most widely used approximations are the local density approximation (LDA) and the generalized gradient approximation (GGA).

The idea behind the LDA comes from the assumption that the electron charge distributions within the system may be treated as homogeneous, i.e., the change in electron density throughout the system is slowly varying. Thus, the functional strictly depends on the density at the coordinate where the functional is to be evaluated,

$$E_{xc}^{LDA}[\rho(\mathbf{r})] = \int \epsilon_{xc}^{LDA}[\rho(\mathbf{r})]\rho(\mathbf{r})d\mathbf{r}, \tag{2.39}$$

where, $\epsilon_{xc}^{LDA}[\rho(\mathbf{r})]$ is the exchange-correlation energy per particle in a homogeneous electron gas. For convenience, we may subdivide $\epsilon_{xc}^{LDA}[\rho(\mathbf{r})]$ into two seperate terms, $\epsilon_{x}^{LDA}[\rho(\mathbf{r})]$ and $\epsilon_{c}^{LDA}[\rho(\mathbf{r})]$. The exchange term is the well-known Dirac expression,

$$\epsilon_{x}^{LDA}[\rho(\mathbf{r})] = -\frac{3}{4}\left(\frac{3\rho}{\pi}\right)^{1/3} = -\frac{3}{4}\left(\frac{9}{4\pi^2}\right)^{1/3}\frac{1}{r_s} = -\frac{0.458}{r_s}, \tag{2.40}$$

where $r_s = ((3\pi\rho)/4)^{1/3}$ is the mean interelectronic distance. The correlation term is approximated using the form suggested by Perdew and Wang [36],

$$\epsilon_{c}^{LDA}[r_s] = -2A(1+\alpha_1 r_s)\ln\left(1+\frac{1}{2AF(r_s)}\right), \tag{2.41}$$

where,

$$F(r_s) = \beta_1 r_s^{1/2} + \beta_2 r_s + \beta_3 r_s^{3/2} + \beta_4 r_s^2. \tag{2.42}$$

The parameters $A, \alpha, \beta_1, \beta_2, \beta_3$ and β_4 are chosen to match various representations of the total electron density [37, 38].

In GGA, the inhomogeneous electron gas is represented, quite generally as,

$$E_{xc}[\rho(\mathbf{r})] = \int \rho(\mathbf{r})\epsilon_{xc}^{LDA}[\rho(\mathbf{r})]F_{xc}(\rho(\mathbf{r}), \vec{\nabla}\rho(\mathbf{r}))d\mathbf{r}, \tag{2.43}$$

where $F_{xc}(\rho(\mathbf{r}), \vec{\nabla}\rho(\mathbf{r}))$ is an enhancement factor that modifies the LDA by taking into account the gradient of the density at the given location in space. The explicit form is still unknown but many attempts have been made to correctly describe it in an analytical form. In this thesis, calculations will be restricted to the use

of the exchange-correlation functional proposed by Perdew, Burke, and Ernzerhof (PBE) [39]. The exact form of the PBE exchange and correlation functionals are provided here so that the reader can appreciate the complexity involved in the creation of these functionals. For the exchange term PBE gives,

$$E_x^{PBE}[\rho(\mathbf{r})] = \int \rho(\mathbf{r})\epsilon_{xc}[\rho(\mathbf{r})]F_x^{PBE}(s(\mathbf{r}))d\mathbf{r}. \tag{2.44}$$

The term, $F_x^{PBE}(s)$, represents an enhancement factor to the local exchange,

$$F_x^{PBE}(s(\mathbf{r})) = 1 + \kappa - \frac{\kappa}{1 + \mu s^2/\kappa}, \tag{2.45}$$

with,

$$s(\mathbf{r}) = \frac{|\nabla\rho(\mathbf{r})|}{2k_F\rho(\mathbf{r})}, \qquad k_F = [3\pi^2\rho(\mathbf{r})]^{1/3}, \qquad \text{and} \qquad \mu = \frac{\beta\pi^2}{3}, \tag{2.46}$$

where k_F is the Fermi momentum, $\beta = 0.066725$, and $\kappa = 0.804$ [39]. This form of the exchange energy uniformly scales the electron density and recovers the homogeneous electron gas limit $F_x(0) = 1$.

The PBE correlation energy,

$$E_c^{PBE}[\rho(\mathbf{r})] = \int \rho(\mathbf{r}) \left[\epsilon_c^{LDA}[\rho(\mathbf{r})] + H_c^{PBE}(\rho(\mathbf{r}), t(\mathbf{r}))\right] d\mathbf{r}, \tag{2.47}$$

with,

$$H_c^{PBE}[\rho(\mathbf{r}), t(\mathbf{r})] = \frac{e^2}{a_0}\gamma\phi^3 \ln\left\{1 + \frac{\beta}{\gamma}t^2\left[\frac{1 + At^2}{1 + At^2 + A^2t^4}\right]\right\}, \tag{2.48}$$

and,

$$A = \frac{\beta}{\gamma}\left[e^{\epsilon_c^{LDA}[\rho]/(\gamma\phi^3/a_0)} - 1\right]^{-1}, \tag{2.49}$$

where $k_s = \sqrt{4k_F/\pi}$ is the Thomas-Fermi screening term, $t(\mathbf{r}) = |\nabla\rho(\mathbf{r})|/(2\phi k_s\rho(\mathbf{r}))$ is a dimensionless density gradient similar to Eq. 2.46 but with a spin scaling factor $\phi(\zeta) = [(1+\zeta)^{2/3}+(1-\zeta)^{2/3}]/2$, and $\gamma = (1-\ln 2)/\pi^2 = 0.031091$ [36, 40]. The advantage of using GGA's over LDA's is that GGA's give very good results for molecular

geometries, bond lengths and ground-state total energies. Current improvements to GGA's involve the use of hybrid functionals, where the exact exchange energy is calculated from Hartree-Fock theory [41–43]. There are also potentially more accurate functionals that include the gradient and the Laplacian (second derivative) terms. These are known as meta-GGA functionals [44, 45]. A nice summary of the most popular functionals can be found elsewhere [46].

2.5 The DMol3 Method

This section will summarize how DFT is implemented for the purpose of this thesis using the DMol3 computer code [47, 48]. Each step in this method will be listed with comments made concerning the specific code used in calculations. A flowchart, is presented so that the reader may better understand the process. Prior to any calculations, the initial atomic coordinates and number of electrons belonging to each atom must be defined. In the present study, this is accomplished by using the program Materials Studio to generate a file containing the xyz coordinates of each atom. In addition, Materials Studio also generates a separate file containing all other input parameters necessary for calculation such as the value for the orbital cutoff radius, the core electron treatment, the type of basis set to use and any tolerance values, for example. Once these files are created and the process starts, DMol3 constructs the molecular orbitals, $\psi_i(\mathbf{r})$, of Eq. 2.31, using a linear combination of atomic orbitals (LCAO),

$$\psi_i(\mathbf{r}) = \sum_{\mu} C_{i\mu}\chi_{\mu}, \tag{2.50}$$

where the $C_{i\mu}$ are the molecular orbital expansion coefficients calculated explicitly by DMol3, and χ_{μ} represents the basis set that describes the atomic orbitals. From this,

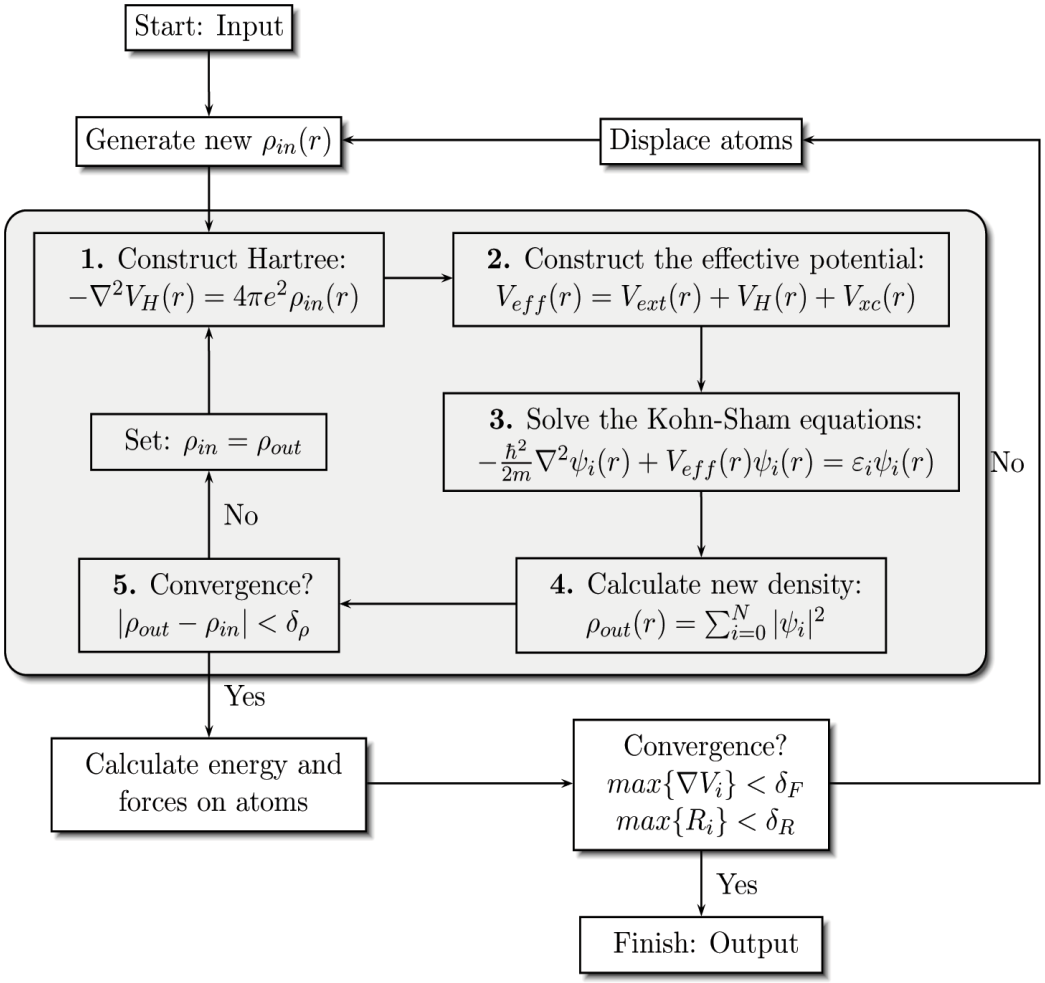

Figure 2.1: DFT Flowchart

an initial charge density is constructed and passed to the self-consistent field (SCF) loop.

1. **Construct Hartree:**

   After constructing the initial charge density the Hartree potential is constructed via Poisson's equation:

   $$-\nabla^2 V_H(\mathbf{r}) = 4\pi e^2 \rho_{in}(\mathbf{r}) \tag{2.51}$$

   This is accomplished by mapping the spherical real space functions onto a three dimensional grid.

2. **Construct the effective potential:**

   The effective potential is computed by summing the three potential energy contributions:

   - The external potential between the electrons and atomic cores
   - The Hartree potential in step
   - The exchange-correlation potential as described in section 2.4.3

3. **Solve the Kohn-Sham Equations:**

   In this step we solve the Schrödinger equation to obtain a new set of atomic orbitals ψ_i with corresponding energies ε_i.

4. **Calculate New Density:**

   Construct the charge density with Eq. 2.37 using the results of Eq. 2.50 and 2.31.

5. **Check SCF convergence:**

   If the difference between the input and output density is less than a predefined threshold then exit the SCF procedure and calculate the total energy of the system along with forces on individual atoms, otherwise set the output density as the new input density and repeat the procedure from step 1.

Once the SCF procedure converges, the forces on the atoms are calculated and then used to determine the amount by which each atomic nucleus must be displaced so as to minimize the total energy of the system. The max force and max displacement tolerances are defined as δ_F and δ_R, respectively. If the maximum force on and displacement of any nucleus is below these tolerances then the system is said to have a stable geometry. At this point, all other output data may be computed, (e.g., three dimensional potential and density profiles, band structure, density of states, work function etc.) If the max force and max displacement are greater than δ_F and δ_R, then a new trial charge density is created using the new positions of the atoms and the SCF procedure starts over.

CHAPTER 3

CLEAN SURFACE PROPERTIES FOR COPPER

3.1 Introduction

In this chapter, clean surface properties of the three lowest index surfaces of copper, namely, Cu(001), Cu(110) and Cu(111) are discussed. The cuts or cleave planes through the copper unit cell, representing these three surfaces, are illustrated in Fig. 3.1.[1]

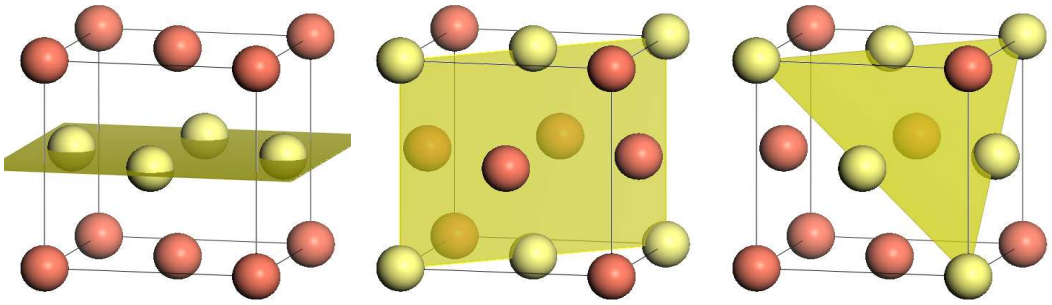

(a) (b) (c)

Figure 3.1: Low index copper surfaces representing the (a) Cu(001), (b) Cu(110), and (c) Cu(111) cleave planes, respectively. The light yellow atoms lie in the surface plane.

All DFT calculations are performed using GGA-PBE as described in Section 2.4.3. The specific code used to solve the DFT calculations was DMol3 which employs fast converging three-dimensional numerical integrations to calculate the matrix elements occurring in the Raleigh-Ritz variational method. The software package,

[1]In general, these are the three lowest index surfaces for any face-centered cubic (fcc) unit cell.

Materials Studio was used to create the files containing the input parameters and initial geometries used by DMol3. All wave functions were expanded in terms of a double-numerical localized basis set which is presently the largest basis set available to DMol3. A real-space cutoff of 5.0 Å and a pseudopotential core electron treatment with scalar relativistic effects was determined to be appropriate for the construction of the basis set.[2] The results for the corresponding bulk parameters, specifically the equilibrium lattice constant and bulk modulus for copper, were found to be 3.65 Å and 130 GPa, respectively. These values are in good agreement with the experimental results of 3.61 Å and 137 GPa [49]. The overestimation of the lattice constant and underestimation of the bulk modulus are also observed in studies of other transition metals [50–52].

3.2 Setup Parameters for Slab Calculations

To simulate the clean surfaces of Cu(001), Cu(110) and Cu(111) a supercell approach consisting of symmetric slabs was utilized. In this approach, the copper unit cell is cleaved normal to the planes shown in fig 3.1 and then periodically extended in the direction normal to the cleave plane by adding atoms until a certain slab thickness is reached. The slab thickness was chosen such that it exceeded at least twice the value of the cutoff radius. Thus, the minimum number of layers, N_l, needed for the Cu(001), Cu(110) and Cu(111) cases were 7, 9, and 7, respectively. These atoms are then placed in a computational cell with a 20 Å thick vacuum on both sides of the slab, 40 Å total. The Brillouin-zone integration was performed using Monkhorst-Pack grids in the irreducible part of the Brillouin-zone [53]. The k-point sampling was chosen such that the spacing for the k-points was approximately 0.02 $Å^{-1}$. The details for each structure are summarized in Table 3.1. Unless otherwise noted, the

[2]The calculations used to make this determination can be found in Appendix A.

total energy, force on atoms, and displacement of atoms for all calculations converged to within 1.0×10^{-5}Hartree, 2.0×10^{-3}Hartree/Å, and 5.0×10^{-3}Å, respectively.[3]

Table 3.1: Setup parameters for Cu(001), Cu(110), and Cu(111). N_l is the layer thickness. SUC is the surface unit cell used for calculation. And BZ are the Brillouin zone parameters

			BZ	
	N_l	SUC	Mesh	k-Points
Cu100	7	1×1	20×20×1	200
Cu110	9	1×1	14×20×1	140
Cu111	7	1×1	24×24×1	288

The Cu(001) surface will be the main surface considered in this thesis. In this chapter, however, the clean surface properties of Cu(110) and Cu(111) will also be computed for comparison. To illustrate these surfaces, the top and side views of the primitive $p(1\times1)$ surface unit cells (SUC) are pictured in Fig. 3.2. The primitive surface vectors $\mathbf{a}_1$ and $\mathbf{a}_2$ are perpendicular in each of the Cu(001) and Cu(110) surface planes whereas in Cu(111) they are separated by an angle of 120°. The magnitudes for the surface vectors are the same for each of the three surfaces ($|\mathbf{a}_1| = |\mathbf{a}_2| = |\mathbf{a}|/\sqrt{2} =$ 2.58Å) except for the Cu(110) surface for which $|\mathbf{a}_1| = |\mathbf{a}| = 3.648$Å, where $|\mathbf{a}|$ is the calculated theoretical lattice constant as determined in Appendix A.3. These surface vectors may be used to extend the (1×1) cells to larger ($m\times n$) cells where m and n are positive integers. The computation time for numerical calculations is, however, minimized by choosing the smallest repeating surface cell but with the requirement that the computational cell be periodic in both surface directions. Beginning with Chapter 4 this topic will be discussed in further detail, where various adsorption

[3] 1 Hartree = 2 Rydbergs = 27.21 eV

coverages require larger computational cells. Since this chapter deals with only clean surfaces, a $p(1\times1)$ surface unit cell is sufficient.

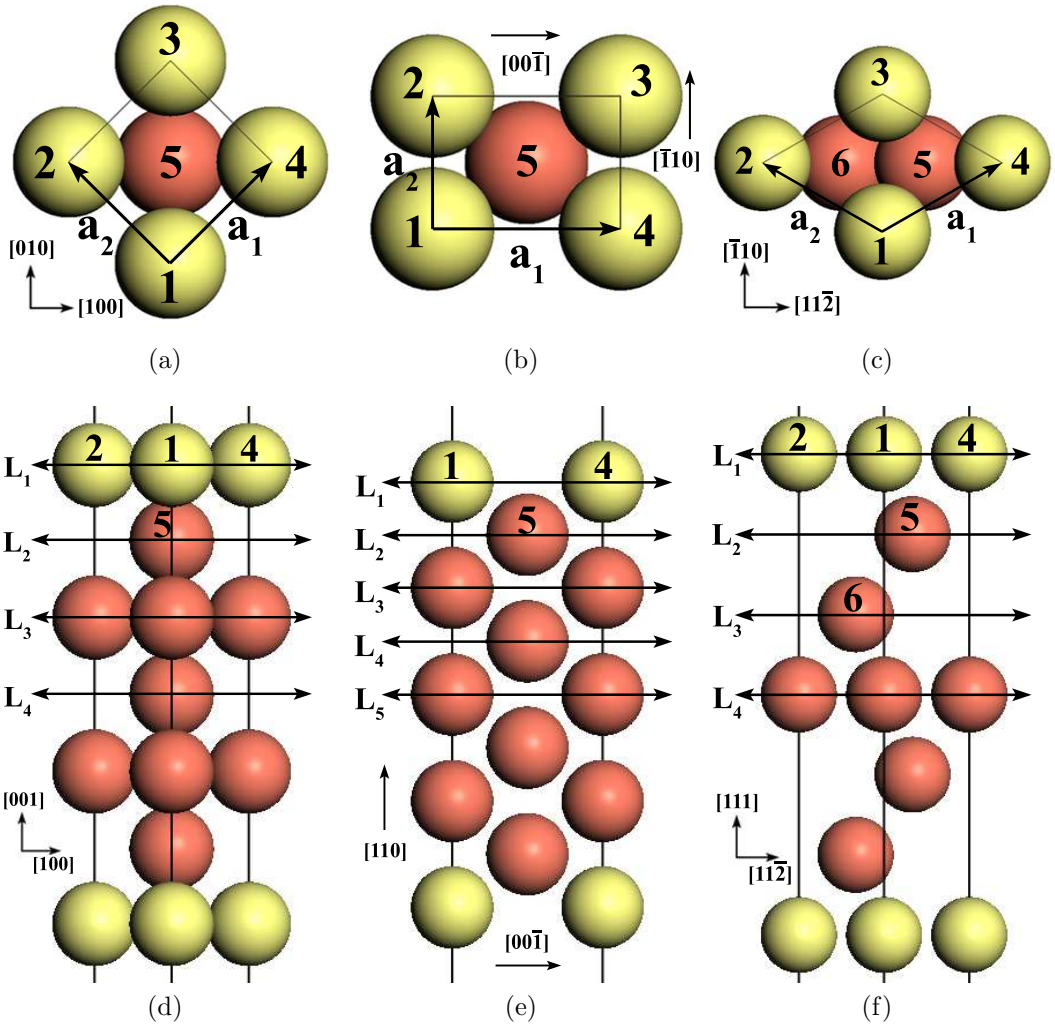

Figure 3.2: Clean copper surface unit cells for Cu(001), Cu(110), and Cu(111) showing the views perpendicular (a,b,c) and parallel (d,e,f) to the surface plane, respectively. Atoms lying in the surface plane are colored light yellow. The vectors $\mathbf{a}_1$ and $\mathbf{a}_2$ are the primitive surface vectors and L_n denotes the nth layer. For all three surface orientations, atoms 1 through 4 lie in L_1 and atom 5 lies in L_2. Due to the hexagonal surface arrangement of Cu(111), atom 6 lies in L_3.

3.3 Geometrical Properties

For a more physically accurate representation of the crystal surface using a slab approach, it is necessary to first find its stable geometry. This process, known as optimization, involves an iterative procedure in which the coordinates of the atoms are adjusted such that total energy of the structure is minimized, i.e., one in which the forces on the atoms are zero.[4] The geometry corresponding to this structure should have a close resemblance to an actual physical structure of the system at equilibrium. In Appendix A, geometry optimization is used to determine the lattice constant of a single unit cell by allowing the dimensions of the unit cell to vary. In the case of slab optimization, the dimensions of the computational cell are held fixed, allowing the atoms to move strictly within the confines of the computational cell. For example, the atoms in the (1×1) surface slabs mentioned in Fig. 3.2 (d), 3.2 (e), and 3.2 (f) will expand or contract in the z direction depending on the charge redistribution effects at the surface. This is a special optimization process known as relaxation. Relaxation is especially important in slab calculations in which the positions of the atoms within the slab must be adjusted so as to accurately represent the physical surface. The significance in relaxing the (1×1) slab initially is that it may be used as a reference slab for future more complex calculations. For example, a single relaxed (1×1) cell can easily be expanded to form a (2×2), (3×3), or even a (4×6) bulk slab. In many cases, the initial relaxing of the clean substrate slab will provide a better initial guess to the system geometry which will in turn lead to faster overall convergence. However, in some cases as will be shown in Section 4.2, this is not always true.

The results of calculations for the relaxed (1×1) surface of Cu(001), Cu(110) and Cu(111) are given in Table 3.2. The + and − signs indicate expansion and contraction of the interlayer spacing, respectively. From these results, it can be seen

[4]The outer loop in (Fig. 2.1) is where this procedure takes place in practice.

Table 3.2: Multilayer relaxations, Δd_{ij}, of the Cu(001), Cu(110), and Cu(111). N_l is the number of layers in the slab. $\Delta d_{ij} = 100(d_{ij}/d_0 - 1)$, where d_{ij} is the interlayer spacing between atomic layers i and j. d_0 is the interlayer spacing in the unrelaxed structure, i.e., d_0=1.821, 1.290, and 2.106Å for Cu(001), Cu(110), and Cu(111), respectively. The + and − signs indicate expansion and contraction of the interlayer spacing, respectively.

Surface	Method	Ref	N_l	$\Delta d_{12}(\%)$	$\Delta d_{23}(\%)$	$\Delta d_{34}(\%)$
Cu(001)	LCAO	TW	7	−1.70	+0.82	+0.49
	FP-LAPW	[54]	7	−2.89	+0.67	+0.38
	PPPW	[19]	7	−3.02	+0.08	−0.24
	LEED	[55]		−1.1 ±0.4	+1.7 ±0.6	
	LEED	[56]		−1.0 ±0.4	+2.0 ±0.8	
	SP-LEED	[57]		−1.2	+0.9	
Cu(110)	LCAO	TW	9	−8.41	+2.84	−1.18
	FP-LAPW	[54]	7	−9.64	+3.62	−0.77
	FP-LAPW	[58]	7	−10.2	+3.8	
	PPPW	[19]	7	−9.27	+2.77	−1.08
	LEED	[59]		−8.5 ±0.6	+2.3 ±0.8	
	LEED	[60]		−10.0 ±2.5	0.0 ±2.5	
	LEED	[61]		−8 ±3		
	LEED	[56]		−7.90	+2.40	
Cu(111)	LCAO	TW	7	−0.39	−0.33	−0.17
	FP-LAPW	[54]	7	−0.56	−0.45	+0.08
	FP-LAPW	[62]	7	−1.19	−0.65	−0.24
	PPPW	[19]	7	−1.27	−0.64	−0.26
	LEED	[63]		−0.3 ±1		
	LEED	[64]		−0.7 ±0.5		

that the separation, d_{12}, between the first and second layers contracts by approximately 1.7% whereas the distances d_{23} and d_{34} expand by approximately 0.82% and 0.49%, respectively. These values are in good agreement with previous results as shown in Table 3.2. Specifically, the relaxation follows the trend of contraction (-), then expansion (+), then expansion(+). The values obtained for the change in interlayer spacing, Δd_{ij}, also fall within the range of previous results. For Cu(111) we observed contraction in each layer. This is not surprising since Cu(111) does

not reconstruct [65]. In summary, the results obtained in this section are in better agreement with experimental values as compared to other computational approaches.

3.4 Work Function

The work function, Φ, of a solid material is a fundamental property that depends sensitively on both the electronic and ionic structure of the material surface. The ionic and electronic potential gradient within the surface layers affects the electronic charge density generated around the ions. Contrariwise, changes in the distribution of the electronic charge density affect the electrostatic surface potential as well as the ionic rearrangement at the surface, and hence the work function. The electrostatic surface potential is sometimes referred to as the double layer because the charge build up at the surface creates an additional barrier through which electrons must pass to escape the crystal. The interplay between the imposed ionic potential and the charge density must thus be obtained self-consistently and thus serves to determine the macroscopic work function.

The work function, Φ, of a solid is defined as the potential energy difference between the Fermi energy of the solid and the potential energy in the vacuum far from the solid surface,

$$\Phi = V_\infty - E_F, \tag{3.1}$$

where V_∞ represents the electrostatic potential energy (EPE) far into the vacuum and E_F is the Fermi energy of the infinite bulk structure. In many cases, energies are referenced to vacuum zero ($V_\infty = 0$) which simply yields,

$$\Phi = -E_F^s, \tag{3.2}$$

where the superscript s labels the Fermi energy as being measured from vacuum zero. The reference energy in DMol3, from which the Fermi energy is given, is ill-defined

due to its dependence on choice of exchange-correlation functional. Thus, the work function must be calculated via Eq. 3.1. Since the copper slab is periodic in the z direction, the middle of the vacuum represents the location farthest away from both sides of the slab. Thus we may define V_∞, the planar average EPE in the middle of the vacuum as,

$$V_\infty = \frac{1}{S} \iint V(x, y, z_\infty)\, dx\, dy, \tag{3.3}$$

where the z axis is chosen perpendicular to the slab surface S and z_∞ refers specifically to the z coordinate in the middle of the vacuum.

Work function, Φ, depends not only on the type of material but also the arrangement of atoms at the surface [66]. There are two common ways of reporting values for the work function. The first is simply reporting the values from the study. Problems can arise however, when considering adsorption. Because of this, looking at the change in work function $\Delta\Phi$ is often more beneficial.

The results for relaxed slab surface work functions are presented in Table 3.3. The values for the work function obtained were 4.49, 4.26, and 4.77 eV for the Cu(001), Cu(110), and the Cu(111) surfaces, respectively. As it follows from results of Table 3.3, these values were on average 0.1 to 0.2 eV lower than the currently accepted experimental values [67]. These results are in line with previous GGA/LDA calculations which also underestimate/overestimate the values of the work function. For example, our calculations for the Cu(111) surface work function agree very well with recent theoretical calculations where the GGA was utilized using the full potential augmented plane wave method [68]. The other results listed in the top section of Table 3.3 use the LDA yielding an overestimation for the value of the work function. The calculations for the work function obtained in this study are in better agreement with experiment than are the other theoretical calculations. For copper, the ordering

of the values obtained for the work function correctly follows surface anisotropy trends from both experimental and theoretical work i.e., the denser the crystal packing, the higher the work function [19, 67, 69–72]. Thus the ordering of the work function for the three lowest index copper surfaces increases as (110 → 001 → 111).

Table 3.3: Summary of Clean Copper Surface Work Functions. The first column represents the theoretical/experimental technique used followed by the reference in the second column. The third, fourth, and fifth columns give work function values for the Cu(001), Cu(110), and Cu(111) surfaces, respectively. The first row of data are results from this work (TW). The remaining methods are defined in the table of acronyms that comes before Chapter 1 of this thesis. All values are in eV.

	Method	Ref	Cu(001)	Cu(110)	Cu(111)
GGA	LCAO	TW	4.49	4.26	4.77
	FP-LAPW	[73]			4.78
	MAPW	[74]	5.21		
LDA	PPPW	[19]	4.95	4.9	5.19
	FP-LMTO	[68]			5.10
	TB-LMTO	[70]	5.26	4.48	5.30
	ARUPS	[69]	4.63 ±0.03		4.93 ±0.03
	Shelton	[71]	4.58	4.4	4.95
	SLEEP	[71]	4.76	4.4	4.95
Experiment	UPS	[75]	4.77 ±0.05		
	PE	[76]			4.85
	PE	[67]	4.59 ±0.03	4.48 ±0.03	4.94 ±0.03

3.5 Density of States

The density of states (DOS), local density of states (LDOS), and partial density of states (PDOS) represent useful semi-qualitative means for analyzing electronic structure. The DOS describes the number of states at each energy level that are

occupied by all electrons in a system. The DOS for a given band n, $N_n(E)$, is defined as,

$$N_n(E) = \frac{1}{4\pi^3} \int \delta(E - E_n(\mathbf{k})\, d\mathbf{k}, \tag{3.4}$$

where $E_n(\mathbf{k})$ describes the dispersion of the given band and the integral is bounded by the Brillouin zone. The total density of states, $N(E)$, is obtained by summation over all bands. The integral of $N(E)$ from minus infinity to the Fermi level gives the total number of electrons in the unit cell. The LDOS is simply the DOS for a single atom or a group of atoms in the system.

The PDOS specifies further the DOS and LDOS by resolving the electronic energy contributions according to their angular momentum. It can also be used to determine whether the energy peaks observed for specific atoms are of s, p, or d character. Furthermore, PDOS can be used to get a qualitative measure on the nature of electron hybridization in the system, or more specifically, the change in hybridization due to the onset of adsorption. The PDOS calculations are based on Mulliken population analysis, which allows the contribution from each energy band to a given atomic orbital to be calculated. Summation of these contributions over all bands produces a weighted DOS. For all PDOS calculation in this thesis, a smearing width of 0.2 eV was used in calculation to help smooth the PDOS curves.

To further stress the importance of PDOS, it is one of the main features observed in XPS, UPS, and optical spectra thus, making it a useful tool for comparison [77]. It can be calculated for single atoms, groups of atoms or all atoms within the DMol3 code, therefore, providing a convenient way to study changes in the electron energy density between neighboring atoms.

The results for the PDOS of the clean copper surface are also presented in this section. For a clean copper slab the PDOS for the 4d electrons peaks at approximately

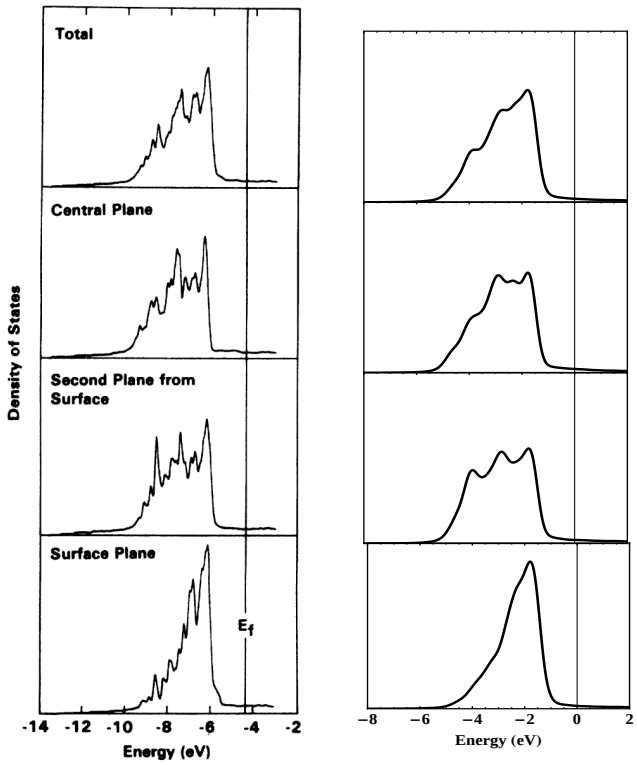

Figure 3.3: Clean Copper Partial Density of States. The PDOS results from Ref. [78] are shown in the four plots on the left while the results from this thesis are shown in the four plots on the right. The smoothed curves in the PDOS plots on the right are a result of usin a smearing width of 0.2 eV in the PDOS calculations. Nevertheless, the peaks still correspond to the plots on the left. The Y axis values are arbitrary units while the X axis values, with respect to the Fermi energy, are in eV.

1.8 eV below the Fermi level as shown in the top right plot of Fig. 3.3. The PDOS for copper surface atoms in the first layer also peak at this value. However, in the second and third layers the 4d orbital PDOS becomes delocalized and additional peaks are formed. These results agree well with previous theoretical results for clean copper surfaces as shown in Fig. 3.3 [78].

CHAPTER 4

LOW COVERAGE OXYGEN ADSORPTION ON CU(001)

In this chapter, a brief introduction including a discussion on supercells and surface coverage will be given in Section 4.1. In Section 4.2 geometrical results for relaxed surfaces will be presented followed by a the results for the electron work function in 4.3. Finally, results obtained for the PDOS, deformation density and difference density will be discussed in Sections 4.4, 4.5, and 4.6.

4.1 Introduction

Studies of oxygen adsorption on copper have been a popular topic of research over the past several decades. It is now widely accepted that for a coverage lower than 0.34 ML, oxygen adsorbs at single sites or, at most, forms $c(2\times2)$ islands [20]. However, some studies have shown the existence of a 0.50 ML $c(2\times2)$ structure [21, 79, 80]. The relaxed Cu(001) structure obtained from Chapter 3 will be used in this chapter to create larger supercells which are necessary to study these different levels of oxygen adsorption.[1] Oxygen atoms were adsorbed on both sides of the slab preserving mirror symmetry. Both surfaces making up the slab were fully relaxed, i.e., all atoms were allowed to move freely without constraint.

Before discussing the results of oxygen adsorption on copper, it is beneficial to summarize the most common adsorption sites used in surface studies. These sites, as illustrated in Fig. 4.1, are unique in that they are highly symmetric about the axis that passes through them normal to the surface plane. Furthermore, notice also that

[1]Results for oxidized Cu(110) and Cu(111) were unavailable during the preparation of this thesis.

Table 4.1: Low coverage structure settings. N_l is the layer thickness. The three Θ values give the total, surface, and subsurface oxygen coverage in monolayers (ML), respectively. SUC is the surface unit cell used for calculation. And BZ are the Brillouin zone parameters

Structure		Surface		BZ	
Name	N_l	Coverage Θ	SUC	Mesh	k points
Cu100+Op3x3	7	0.11	3×3	8×8×1	32
Cu100+Op2x2	7	0.25	2×2	10×10×1	50
Cu100+Oc2x2	7	0.50	2×2	10×10×1	50

Fig. 4.1 (a) is similar to Fig. 3.2 (a) as far as atom numbering and view plane are concerned, but different in that Fig. 4.1 (a) has been rotated clockwise 45° and its even numbered planes have been expanded by $|\mathbf{a}_1|$ and $|\mathbf{a}_2|$ in the $\mathbf{a}_1$ and $\mathbf{a}_2$ directions, respectively. For example, atoms one, two, three, and four are surface atoms that make up the first substrate layer L_1 whereas atoms five and six are sub-surface atoms residing in L_2. In Fig. 4.1 (a), the arrows (b) and (c) give the direction of views for Fig. 4.1 (b) and 4.1 (c), respectively.

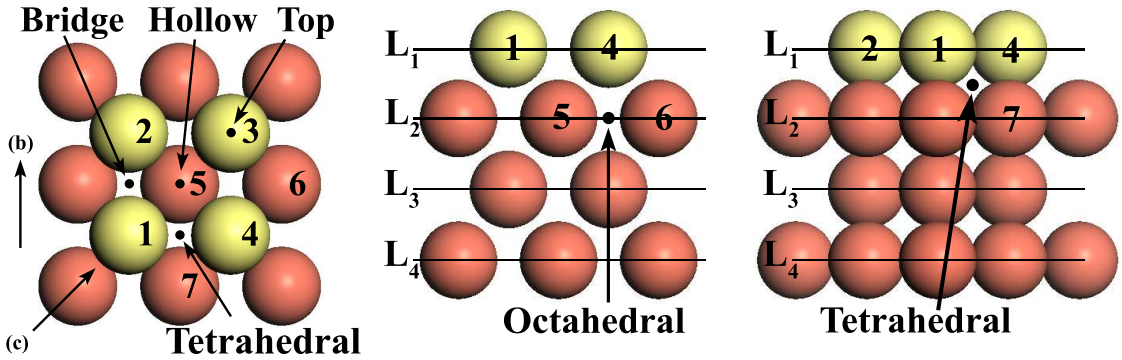

(a) (b) (c)

Figure 4.1: Symmetric adsorption sites for Cu(001) showing the (a) view from above, (b) side view, and (c) side view rotated by 45°. Yellow atoms represent copper atoms in the topmost layer.

The three most common sites for surface adsorption are the top, bridge and hollow sites. An adatom placed above the first layer, L_1, directly above any of the topmost substrate atoms (e.g., atom 1, 2, 3 or 4 etc.) is said to reside at the top site.[2] An adatom placed halfway between two neighboring surface atoms (e.g., atom 1-2, 2-3, 3-4 or 4-1, etc.) and above the first layer is said to occupy the bridge site because it essentially forms a bridge between the two underlying atoms. The third surface site, called the hollow site resides above L_1 directly over site five. As it will be shown later in this thesis, an adatom at this site bonds to its four lower lying copper atoms in L_1 but not to the fifth copper atom directly underneath. In previous studies, it has been found that the most energetically favorable site for single atom adsorption on an fcc(100) surface is the hollow site [21, 22]. For this reason, the bridge and top sites will not be covered in this thesis.

There are also two types of sub-surface adsorption sites called the octahedral and tetrahedral sites. An octahedral site, such as the one pictured in Fig. 4.1 (b), represents the location in the L_2 plane directly underneath any of the L_1 surface atoms. Another example of an octahedral site would lie in L_3 directly under atom five. In this study, however, any adatoms occupying sub-surface octahedral sites will go no deeper than L_2. The second sub-surface site known as the tetrahedral site, can be found directly under any of the surface bridge sites half way between L_1 and L_2 as shown in Fig. 4.1 (a) and 4.1 (c). An adatom located at a tetrahedral site usually bonds to its four nearest neighbor substrate atoms. For example, an adatom at a tetrahedral site directly below the 3-4 bridge site would be tetrahedrally bonded to atoms three, four, five, and six.

The lowest level of coverage considered in this thesis for oxygen adsorption on Cu(001) is shown in Fig. 4.2 (a). In this structure, oxygen atoms are spaced at

[2]Adsorbate atoms are commonly referred to as adatoms.

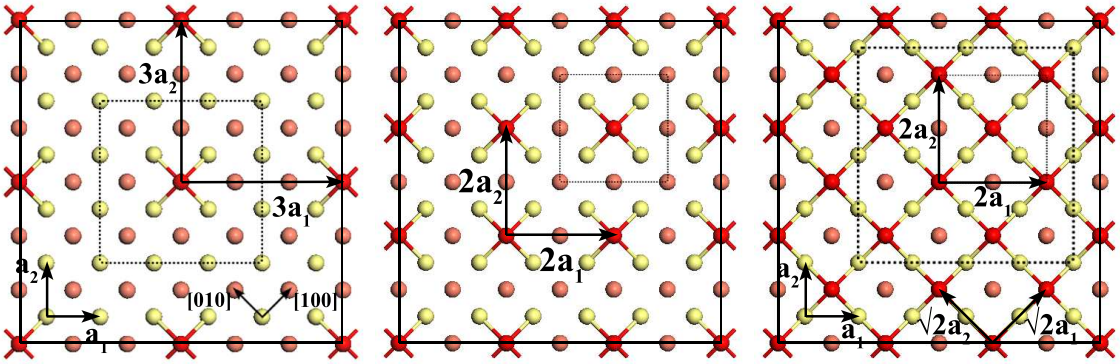

(a) (b) (c)

Figure 4.2: Low coverage oxidation sites for the (a) Cu(001)-$p(3\times3)$, (b) Cu(001)-$p(2\times2)$, and (c) Cu(001)-$c(2\times2)$ phases. Yellow atoms represent copper atoms in the topmost layer.

$3|\mathbf{a}_1|$ and $3|\mathbf{a}_2|$ intervals in the $\mathbf{a}_1$ and $\mathbf{a}_2$ directions, respectively. The minimum SUC needed to correctly represent the periodic nature of such a spacing is a $p(3\times3)$ SUC as illustrated by the dotted boarder in Fig. 4.2 (a). The amount of coverage can be calculated easily by dividing the number of adsorbate (oxygen) atoms present by the number of primitive unit surface cells comprising the overall computational cell. Since $p(3\times3)$ contains $3\times3=9$ primitive cells, then $1/9=0.11$ML is the oxygen coverage for this computational cell. The $p(3\times3)$ supercell is constructed as a collection of nine identical $p(1\times1)$ SUC's using the methods discussed in Sec. 3.2. In reality, any of the nine hollow sites could be used for calculation, however the symmetry of the computational cell will be highest with the oxygen adatom placed just above the surface at the centermost fourfold hollow site on both sides of the slab.[3]

A value between one and two Angstroms is chosen as an initial guess to the height at which to place the oxygen atom above the surface. The earlier discussed approach is also used to determine the coverage for the $p(2\times2)$ structure, Fig. 4.2 (b)

[3]The term highest symmetry used here means the computational cell preserves mirror, rotation ($\pi/2$), and inversion symmetry about each x, y, and z axis.

and the $c(2\times2)$ structure, Fig. 4.2 (c). The $c(2\times2)$ structure is classified as a *centered* (2×2) structure with an additional adsorbate atom placed at the center of the $p(2\times2)$ surface cell. This structure can also be classified in the primitive unit cell notation as, $(\sqrt{2}\times\sqrt{2})$R45°. In this notation, the adsorbate unit cell is rotated 45° degrees with respect to the substrate unit cell and its surface vectors are $\sqrt{2}$ times larger in magnitude. The $c(2\times2)$ notation is used here because of its convenience, however, as will be shown in Section 5.1, this notation is not always appropriate and hence the primitive cell notation must be used.

4.2 Geometrical Properties

A portion of the optimization results obtained for these three structures is given in Table 4.2. The results of calculation for the Cu-O bond length, d_{Cu-O}, and height, h_O, of oxygen above the surface are in excellent agreement with previous results for the 0.25 and 0.50 ML coverage cases [22–24, 79, 81, 82]. Note that the results for d_{Cu-O} and h_O obtained for the 0.11 ML coverage are new. The results for d_{Cu-O} are found to decrease with increasing coverage following the correct trend. and their values follow the correct trend, i.e., as oxygen adsorption increases, the bond lengths get shorter and the height of the oxygen adatom above the copper surface decreases. This is caused by slight displacements of the nearest neighbor copper atoms in the xy plane in a direction away from the oxygen atom. As a result, the oxygen atom adsorbs closer to the surface layer.

The same trend is expected for h_O however in the 0.11 ML case, the oxygen height is slightly lower than in the 0.25 ML case. This is easily explained as the oxygen atom in the 0.11 ML case is able to adsorb closer to the surface layer due to small outward displacements of its nearest neighbor copper atoms in the xy plane just beneath it.

Table 4.2: Oxidized Cu(001) surface geometrical properties. The first column gives the coverage in ML. d_{Cu-O} is the distance from the surface adsorbed oxygen atom to nearest neighbor copper atom and h_O is the height of the oxygen atom above the first copper layer. Δd_{ij} represents the percent change in interlayer spacing with respect to the unrelaxed (relaxed) clean copper surface. The values in parenthesis represent the percent change in interlayer spacing of the form, $\Delta d_{ij} = 100(d_{ij}/d_{ij}^{rel} - 1)$, where d_{ij} now represents the "average" interlayer spacing and d_{ij}^{rel} represents the the interlayer spacing from the relaxed copper surface obtained in Section. 3.3.

ML	d_{Cu-O}(Å)	h_O(Å)	Δd_{12}(%)	Δd_{23}(%)	Δd_{34}(%)
0.11	2.011	0.794	+0.055(+2.1)	−0.55 (−0.82)	+0.00 (+0.00)
0.25	2.008	0.822	+0.71 (+2.8)	+0.22 (−0.05)	+0.16 (+0.16)
0.50	1.946	0.678	+8.9 (+11.1)	−1.8 (−2.1)	+0.49 (+0.49)

The calculated results of the interlayer spacing between consecutive copper layers is also shown in Table 4.2. However, upon relaxation it was found that the displacements corresponding to each of the copper atoms shifted non-uniformly in the z-direction. For example, the copper atom in L_2, lying directly below the oxygen adatom, shifted slightly toward the center of the slab whereas the other copper atoms in L_2 shifted upward toward the vacuum. Therefore, the location of the plane which corresponded to the average height of copper atoms in a given layer was used in calculation of the interlayer spacing. Also provided in Table 4.2 are the calculated values of Δd_{ij} shown in parenthesis which correspond to,

$$\Delta d_{ij} = 100(d_{ij}/d_{ij}^{rel} - 1), \tag{4.1}$$

where d_{ij} now represents the "average" interlayer spacing and d_{ij}^{rel} represents the the interlayer spacing from the results of the relaxed copper surface obtained in Section. 3.3. From these results it is easy to see that while the change in interlayer spacing is relatively small for the 0.11 and 0.25 ML cases, it is significantly larger for the 0.50 ML case. Moreover, the results obtained from calculations using the clean unrelaxed copper slab in comparison to the results obtained when using the re-

laxed copper slab, indicated that the unrelaxed slab is a better choice for calculations particularly for the case when oxygen adsorbs on copper.

4.3 Work Function

The results of calculation for the work function, regarding the three low coverage oxygen adsorbed structures, discussed in this chapter are presented in Table 4.3. These results were obtained using the same methods presented in Section 3.4. To

Table 4.3: Oxidized Cu100 Surface Work Functions. The second row gives the coverage in ML. Work function values are in eV.

	clean	p3x3	p2x2	c2x2
Coverage Θ	0.00	0.11	0.25	0.50
Work Function Φ	4.49	4.80	5.19	5.44

study the relationship between work function and adsorption coverage, it is useful to look at the change in work function, $\Delta\Phi = \Phi - \Phi_{clean}$, as a function of adsorbate coverage as given in Fig. 4.3, rather than the actual value obtained from calculation. The graph of Fig. 4.3 illustrates this by showing a linear increase in the work function up to 0.25 ML, with a slightly less increase from 0.25 to 0.50 ML. If follows from table 4.3 that the largest value of Φ for the oxidized Cu(001) surface corresponds to the 0.5 ML oxygen coverage.

4.4 Density of States

The PDOS results for the three low coverage cases considered in this study are shown in Fig. 4.4. In each of the three plots, the dashed line represents the oxygen p-state, while the solid red line represents the d-state belonging to one of the nearest neighbor copper atoms, and the solid blue line represents the d-state corresponding

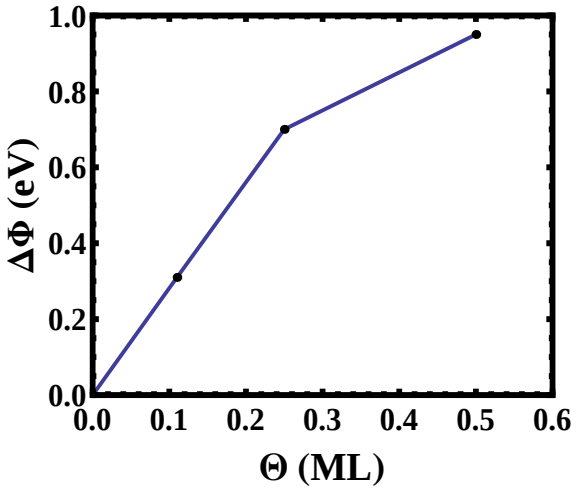

Figure 4.3: Low coverage work functions for Cu(001)

to the copper atom directly underneath the oxygen atom. All energy measurements are taken with respect to the Fermi level represented by the thin vertical black line at $x = 0$. The same methods used in Section 3.5 to calculate the copper PDOS are used here.

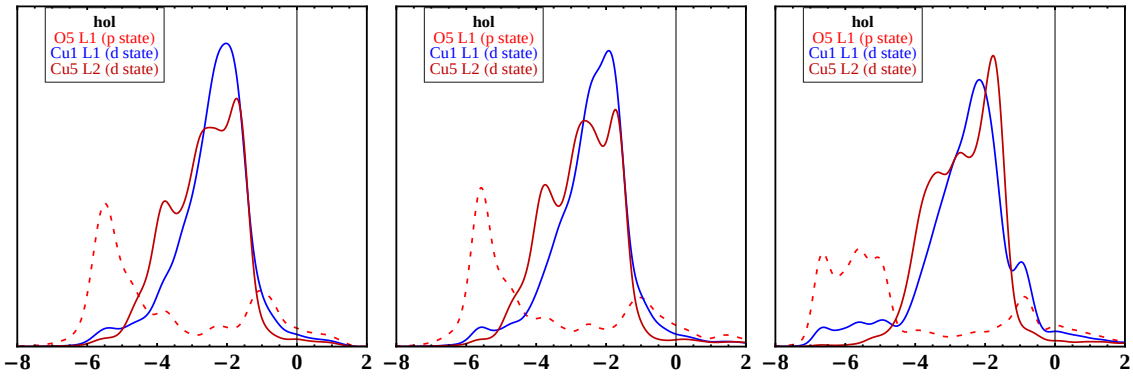

Figure 4.4: Low coverage partial density of states for (a) Cu(001)-$p(3\times3)$, (b) Cu(001)-$p(2\times2)$, and (c) Cu(001)-$c(2\times2)$. The dashed line represents the oxygen p-state and the solid lines represent the copper d-state. Y axis units are arbitrary, whereas X axis units are in eV and are given with respect to the Fermi level.

It follows from Figs. 4.4 (a) and 4.4 (b) for the 0.11 ML and 0.25 ML cases, that oxygen has a distinct peak at approximately -6.0 eV below the Fermi level, while in the 0.50 ML case the oxygen peak decreases and broadens out to a range of approximately -7.0 to -5.0 eV. In all three cases, however, the copper d-state that contributes most to the PDOS at these oxygen coverages are the ones belonging to the nearest neighbor copper surface atoms. This suggests that the majority of the Cu-O bonding takes place between the oxygen atom and the surface layer copper atoms and not with the sub-surface copper atoms which should lead to increased electron accumulation at the oxygen site. These results are in good agreement with previous results [25, 83].

4.5 Deformation Density

One way to study the nature of bonding and charge transfer effects is to consider the deformation density of a given system. The deformation density, $\rho^{\Delta'}$, is computed by subtracting separately the charge densities for each atom in the system from the total charge density of the system,

$$\rho^{\Delta'}(\mathbf{r}) = \rho^{Cu+O}(\mathbf{r}) - \sum_{i}^{M} \rho^{Cu_i}(\mathbf{r}) - \sum_{j}^{N} \rho^{O_j}(\mathbf{r}), \tag{4.2}$$

where $\rho^{Cu+O}(\mathbf{r})$ is the total electron density of the substrate adsorbate system, $\rho^{Cu_i}(\mathbf{r})$ and ρ^{O_j} are the charge densities of the ith copper atom and jth oxygen atom, respectively. The total number of copper and oxygen atoms in the computational cell are represented by M and N, respectively. For all deformation density plots in this thesis, the contours are separated at $2.5\times10^{-3}\,\mathrm{elec/\AA^3}$ intervals ranging from $\pm0.1\,\mathrm{elec/\AA^3}$.

It follows from the results obtained for the deformation density presented in Fig. 4.5 that there is distinct charge depletion close to each of the bulk copper nuclei with a mild charge accumulation in the interstitial regions. This is characteristic of

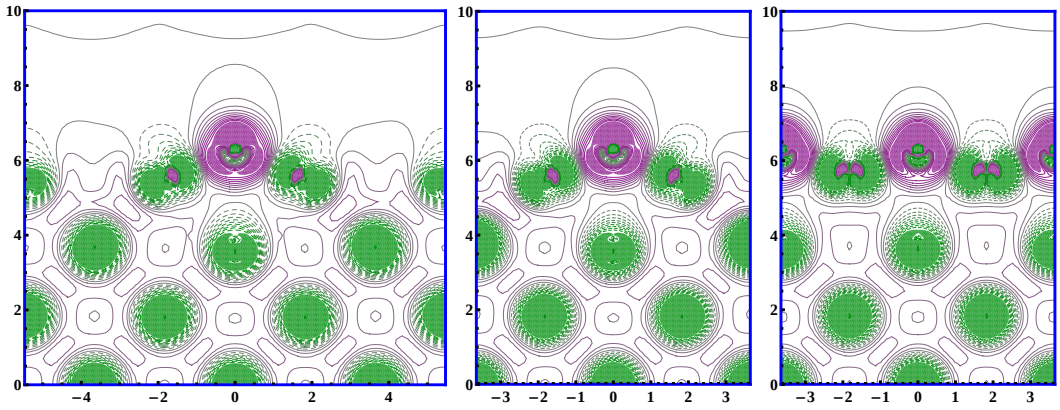

Figure 4.5: Low coverage deformation density plots, $\rho^{\Delta'}$, for (a) Cu(001)-p(3×3), (b) Cu(001)-p(2×2), and (c) Cu(001)-c(2×2). All plots are viewed perpendicular to the plane containing the O-Cu-O bond. Solid (violet) contours represent regions of charge accumulation, while dashed (green) lines represent regions of charge depletion. Contours lines are drawn at 2.5×10^{-3} elec/Å^3 intervals ranging from ±0.1 elec/Å^3.

metallic bonding where the valence electrons become delocalized from their original atom and are essentially free to move throughout the lattice. It also follows from Fig. 4.5 that most of the charge accumulation takes place around the adsorbed oxygen atom. The distorted deformation density seen in the first layer of copper atoms suggest that this accumulation is a result of charge transfer primarily from surface copper atoms to the adsorbed oxygen atom.

One of the major drawbacks concerning the deformation density is that interaction effects between electrons of neighboring atoms are not taken into consideration when performing the summations. This makes it difficult to study accurately the effects of charge transfer before and after oxygen adsorption. However, a similar method of calculation known as the difference electron density, provides an alternate way to more accurately study these effects.

4.6 Difference Electron Density

The difference electron density, ρ^{Δ}, is similar to $\rho^{\Delta'}$ except $\rho^{Cu}(\mathbf{r})$ is recalculated using the geometrical results of $\rho^{Cu+O}(\mathbf{r})$ but with the adsorbate atoms removed and $\rho^{O}(\mathbf{r})$ is recalculated the same way using the results of $\rho^{Cu+O}(\mathbf{r})$ but with the all substrate copper atoms removed. Thus, the difference electron density is given as,

$$\rho^{\Delta}(\mathbf{r}) = \rho^{Cu+O}(\mathbf{r}) - \rho^{Cu}(\mathbf{r}) - \rho^{O}(\mathbf{r}). \tag{4.3}$$

In all three cases the positions of the atoms are held fixed to the positions of the original relaxed adsorbate/substrate system. The solid purple and dotted green contours in Fig 4.5 and 4.6 represent regions of charge accumulation and depletion, respectively. Contours are separated by $\pm 0.1\,\mathrm{elec/\AA^3}$ with the solid saturated regions representing values of ρ^{Δ} that fall outside this range. In order to enhance the regions of accumulation and depletion in the difference electron density plots, a factor of ρ^3 was used to in separating the contours [25, 74].

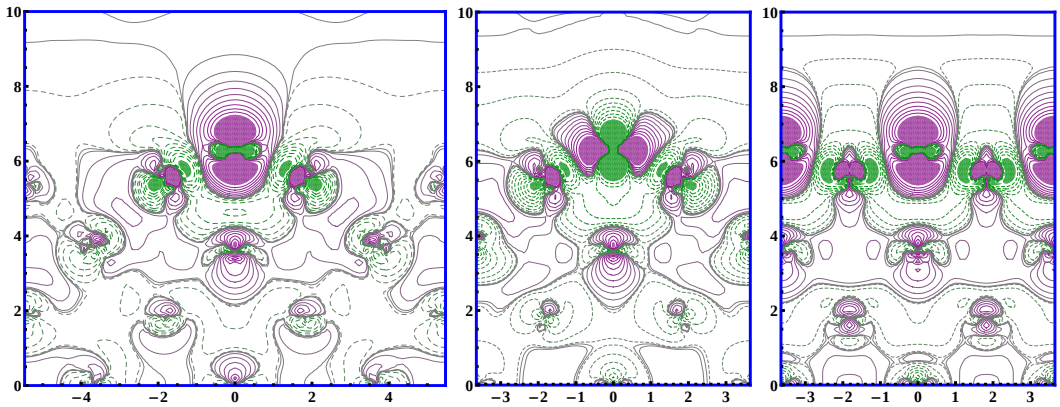

(a) (b) (c)

Figure 4.6: Low coverage difference density plots, ρ^{Δ}, for (a) Cu(001)-p(3×3), (b) Cu(001)-p(2×2), and (c) Cu(001)-c(2×2). All plots are viewed perpendicular to the plane containing the O-Cu-O bond. Solid (violet) contours represent regions of charge accumulation, while dashed (green) lines represent regions of charge depletion. Contours range from $\pm 0.1\,\mathrm{elec/\AA^3}$ and are separated by a factor of ρ^3

The results from the difference density plots give a somewhat different picture of the charge redistribution. In the bulk region the metallic bonding nature of neighboring copper atoms is not obvious. Instead, subtle changes in the charge distributions are now apparent. For example, in Fig. 4.6 (a), the charge distribution in the immediate vicinity of the copper atom located at position $(x, y) \approx (2, 2)$ has been shifted slightly toward the surface as indicated by the solid purple contours. There is also a corresponding region of charge depletion just below the atom as indicated by the dashed green contours. However, this is not always the case. The copper atom located at position $(x, y) \approx (0, 3.5)$ shows charge accumulation both above and below the atom with a slightly smaller region of charge depletion to the right and left. With the exception of Fig. 4.6 (b), the results of calculations pertaining to the surface layer look very similar to those obtained from the deformation density. There is an obvious charge accumulation in the vicinity of the oxygen atom and a charge depletion occurring just outside the copper atom along the line connecting them. This further suggests that the charge transfer effects observed, take place primarily between the oxygen atom and the copper atoms in the first surface layer. The behavior of the difference electron density around the oxygen atom and lower lying layers observed in Figs. 4.6 (a), (b), and (c) will be explored in future studies.

Because the calculation for $\rho^{Cu}(\mathbf{r})$ was performed on all the copper atoms at once, the correlation effects were taken into account thus showing little difference between the density of bulk copper atoms in $\rho^{Cu+O}(\mathbf{r})$. This also makes the difference electron density very sensitive to small amounts of electron transfer. Thus, the difference density provides a useful tool in examining the changes in surface and sub-surface charge redistribution arising specifically from adsorption.

One of the things that needs to be taken into consideration in the difference electron density calculation is the fact that when performing the calculation for the

copper only slab, the atoms are not in their most geometrically stable configuration. As a result, the charge density arising from such a calculation gives theoretically correct results obtained without full optimization of the structure. Therefore, the deformation and difference densities both have their own advantages and should always be used in conjunction with other physical parameters whenever drawing conclusions concerning the properties of quantum systems.

Based on observations of the deformation and difference density plots presented in this section, it appears that the increase in work function observed in Section. 4.3 can be attributed to charge transfer effects from the surface copper atoms to the adsorbed oxygen atoms.

CHAPTER 5

HIGH COVERAGE OXYGEN ADSORPTION ON CU(001)

In this chapter, we will explore the process of oxidation for high adsorbate coverages ranging from 0.50 to 1.50 ML. Section 5.1 will give an introduction followed by a brief description in Section 5.2 of the specific high coverage structures studied. The remaining sections will contain the results of calculations for geometrical relaxation and reconstruction parameters, deformation and difference density profiles, density of states, and values of the work function.

5.1 Introduction

Studies of oxygen adsorption on Cu(001) have been a popular topic of research, discussion and debate over the past several decades, mainly due to the elusive nature of adsorption geometry above 0.25 ML oxygen coverage. In the past, two possible structures representing an oxygen coverage of 0.50 ML have been suggested. The first of these, the $c(2\times2)$ structure was discussed previously in Chapter 4. The second structure, known as the missing row structure or MR for short, may be represented by using a $c(2\times2)$ oxygen overlayer expanded out to a $p(4\times4)$ SUC as outlined by the dashed border in both Figs. 4.2 (c) and 5.1. The MR structure is similar to the $c(2\times2)$ structure but with the fourth row of copper atoms (those with red X's) removed. However, the MR structure can be represented also through the use of a $(2\sqrt{2}\times\sqrt{2})R45^\circ$ surface cell as shown by the solid rectangle in Fig. 5.1.

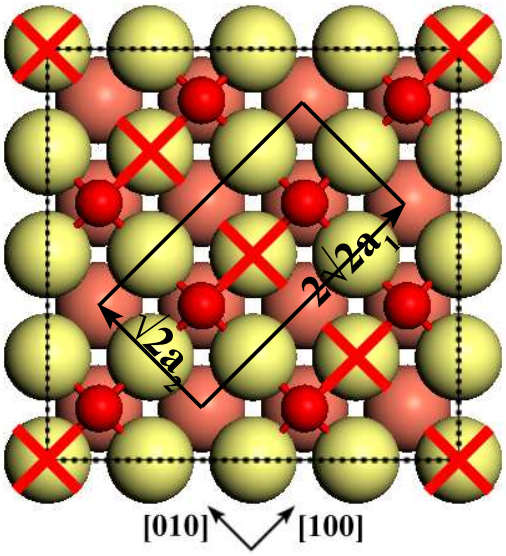

Figure 5.1: The supercell (dotted border) and reduced cell (solid border) of the 0.50ML missing row structure. This structure is taken from where the $c(2\times2)$ overlayer is represented on a $p(4\times4)$ periodic primitive surface cell arrangement of copper atoms. The yellow atoms represent copper atoms in the topmost layer. The missing row structure is obtained when the fourth row copper atoms (marked with red X's) are deleted.

Some experiments (Ref. [21, 79, 80, 82]) have shown the presence of the $c(2\times2)$ phase whereas others (Ref. [26, 84–88]) have shown the existence of the MR phase.[1] Additionally, some theoretical studies suggest that the MR phase is energetically more favorable than the $c(2\times2)$ phase [81, 89]. To explain the reconstruction that takes place between 0.25 and 0.50 ML coverage, it has been suggested that the missing copper atoms are actually ejected from the surface and reattached to some remote location due partially to long-range Coulombic interactions [20]. The growing consensus regarding the 0.50 ML oxygen covered copper surface is that the $c(2\times2)$ structure is unstable. It is now widely accepted that for low coverages, oxygen adsorbs at single hollow sites or, at most, forms $c(2\times2)$ islands up to 0.33 ML and at coverages

[1]The $(2\sqrt{2}\times\sqrt{2})R45^\circ$ structure will be referred to as the missing row structure or MR for short.

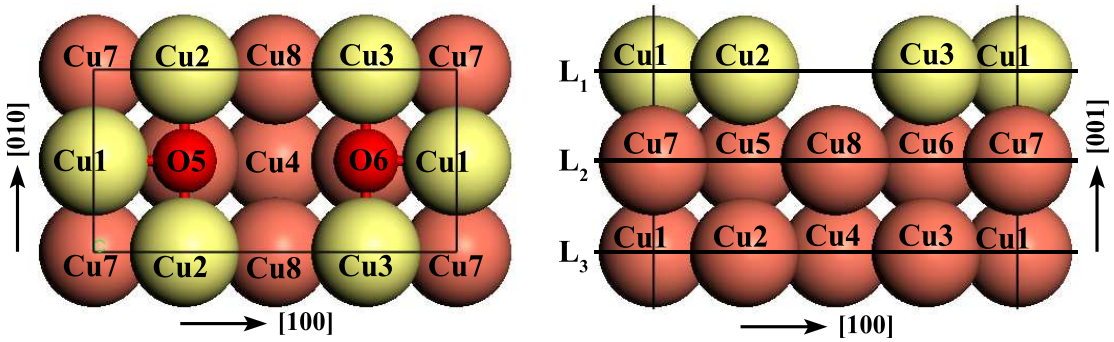

(a) (b)

Figure 5.2: The 0.50 ML missing row structure as viewed from the (a) top and (b) side. The yellow atoms represent copper atoms in the topmost layer. The nomenclature used to label the atoms is the standard convention used for all structures presented in this chapter. See the text in this section for more details.

between 0.34 to 0.50 ML, the surface experiences missing row reconstruction. In this chapter, the process of oxidation for coverages ranging from 0.50 to 1.50 ML will be explored.

Recently, Kangas et al. performed calculations for reconstructed phases involving high coverage oxygen adsorption based on the MR structure [22, 27]. In their study, they considered different coverages of oxygen adsorption ranging from 0.50 to 1.50 ML surface/sub-surface coverage mixtures. These mixtures involve mostly oxygen atoms placed at surface hollow and sub-surface octahedral sites. This chapter focuses on the structures obtained in their study that had the lowest adsorption energy at each stage of oxidation. All structures considered in this chapter were fully relaxed using the results of Ref. [27] as an initial guess geometry. The same input parameters that were used in chapter 4 are used in this chapter with the exception of the Brillouin zone parameters where a 7×14×1 k-point mesh corresponding to 49 k-points was used in all calculations.

5.2 Geometrical Properties

For a coverage of 0.75 ML, the configuration that yielded the lowest adsorption energy was the hol7 structure [27]. This structure is formed by placing an oxygen atom at the hollow site directly above the Cu7 atom as shown in fig 5.3 (a). The structure that gave the lowest adsorption energy for the 1.0 ML case corresponded to the octa23 structure. In this configuration, shown in Fig. 5.3 (c), the two original MR

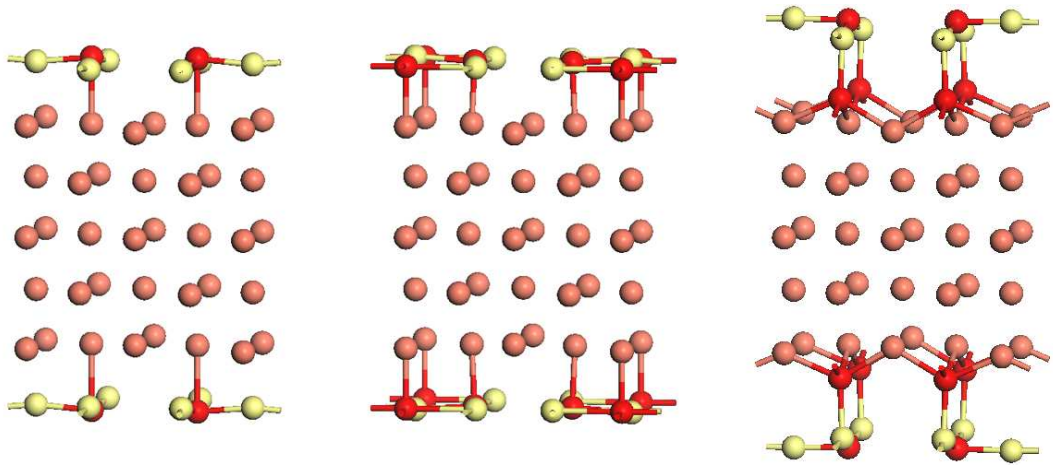

(a) (b) (c)

Figure 5.3: Calculated high coverage atomic structures for the (a) missing row, (b) hol7, and (c) octa23 structures. See Fig. 5.2 for the numbering.

oxygen atoms are accompanied by two additional sub-surface oxygen atoms sitting at the octahedral sites directly under the first layer Cu2 and Cu3 atoms. After relaxing this structure, it was found that the position of the sub-surface oxygen atoms shifted toward the surface causing the average separation between layer 1 and layer 2 to increase by approximately 50%.

Two structures corresponding to 1.25 ML coverage of adsorbed oxygen with the lowest adsorption energies were considered in this chapter. The hol7octa23 structure which is similar to the hol7 structure, in that it has a 0.75 ML surface coverage but

with an additional 0.50 ML sub-surface coverage at the octa23 sites. The octa123 structure has the original MR surface coverage of 0.50 ML but with an additional sub-surface coverage of 0.75 ML with three oxygen atoms placed at octahedral sites.

Upon successful relaxation of the hol7octa23 structure, it was found that the geometry of this relaxed structure did not resemble the results obtained in Ref. [27]. Specifically, the Cu7 atom relaxed to a position nearly coplanar to the octa23 atoms as shown in Fig. 5.4 (a), whereas Kangas et al. show the relaxation of the Cu7 atom

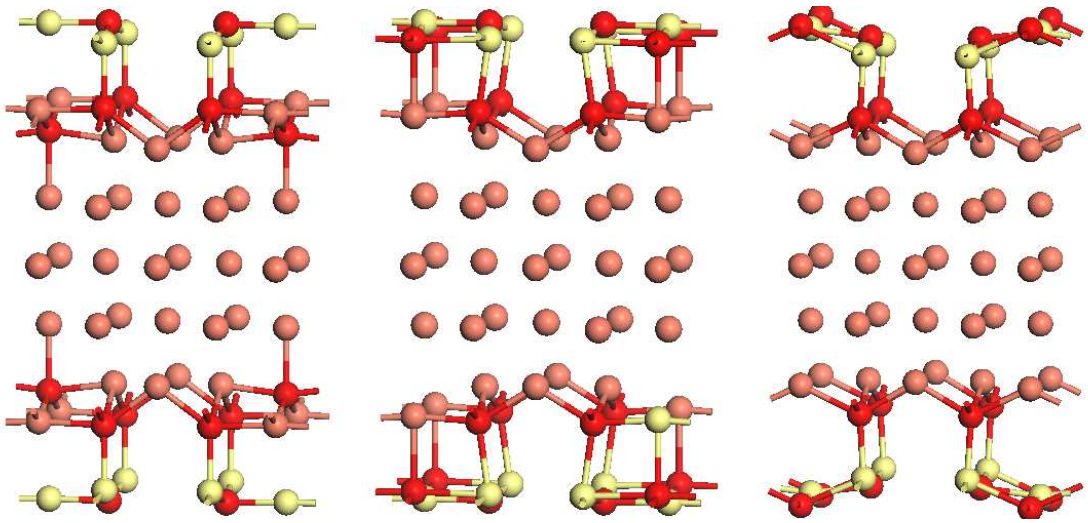

(a) (b) (c)

Figure 5.4: Calculated high coverage atomic structures for the (a) hol7octa23, (b) hol7octa23k, and (c) octa123 structures. See Fig. 5.2 for the numbering.

to be coplanar to the rest of the copper atoms in the second layer. Another noticeable difference was the position of the oxygen O7 atom which relaxed to a point just below the plane containing the topmost Cu1 atom and nearly co-planar to the Cu2 (and Cu3) atom(s). According to the results obtained in Ref. [27], the position of the O7 atom was found to lie at a point just above the Cu1 surface plane. Consequently, the $Cu7 - O7$ bond length resembling the hol7octa23k structure obtained in Ref. [27] is

approximately 70% larger than the initial hol7octa23 results obtained in this thesis.[2] In order to obtain a relaxed atomic configuration similar to the one found in Ref. [27], a second calculation was performed using the geometry of Fig. 5.4 (b) as an initial guess but rearranging the positions of the Cu7 and O7 atoms using a more rigorous form of geometrical analysis to extrapolate the actual atomic positions from the original paper [27]. The final relaxed structure, the so called hol7octa23k structure, is shown in Fig. 5.4 (c).

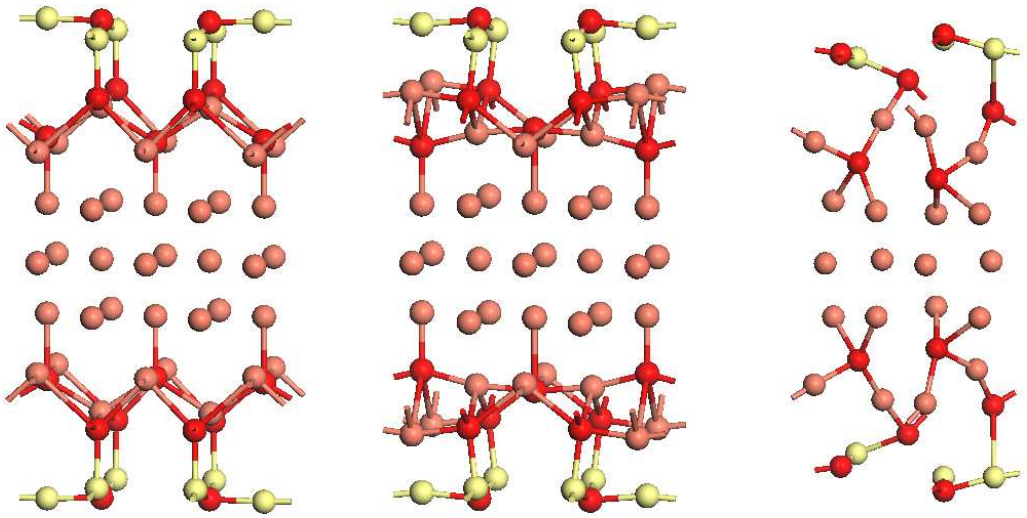

(a) (b) (c)

Figure 5.5: Calculated high coverage atomic structures for the (a) octa1234, (b) octa1234k, and (c) oxide structures. See Fig. 5.2 for the numbering.

Two structures corresponding to the coverage of 1.50 ML also resulted in lowest adsorption energy values. The octa1234 structure which has oxygen atoms at all four second layer octahedral sites and an oxide structure containing oxygen atoms at tetrahedral sites between layers. The results of calculation for the optimized oxide

[2]To distinguish between these two structures, a "k" has been added to the structure most closely resembling the one found in Ref. [27].

structure were very bad as can be seen in Fig. 5.5. Therefore the results will not be included in this chapter.

From the results of the relaxed octa1234 structure, the two octa23 oxygen atoms moved above the second layer of copper atoms which itself moved above the octa14 oxygen atoms thereby forming a third sub-surface oxygen layer. Similar geometrical discrepancies that were observed between the hol7octa23 and hol7octa23k structures were also observed between the initial results of this thesis and Ref. [27]. The most noticeable of these discrepancies was in the final relaxed position of the Cu7 atom in the third oxygen layer. According to the calculations of Kangas et al., this atom lies in the second layer coplanar with the octa23 oxygen atoms. Therefore, the same technique used to obtain the hol7octa23k structure was used to find the so called octa1234k structure. The geometrical results of the octa1234 and octa1234k structures are shown in Fig. 5.5 (a) and 5.5 (a), respectively. The second structure considered for the 1.50 ML case was the oxide structure.

A portion of the results obtained through the geometry optimization of the structures discussed in this chapter are given in Table 5.1. The nomenclature on the atoms in the first and second column are to be referenced with Fig. 5.2. For example, the first bond length value presented in the table, 1.879 Å, refers to the distance between the Cu1 atom and the O5 adatom atom or $Cu1 - O5$. This distance also represents the $Cu1 - O6$ bond length due to mirror symmetry in the vertical [100] plane containing the Cu4 atom. The rest of the table follows from these same rules. The results given in Table 5.1 correspond directly to each of the structures shown in Figs 5.3, 5.4, and 5.5.

Table 5.1: High coverage Cu(001) missing mow Cu-O bond lengths. The first row gives the structure name while the second, third, and fourth rows give the surface, sub-surface and total coverage in ML, respectively. The nomenclature for the terms in the first and second columns should be used in connection with Fig. 5.2. The values in parenthesis correspond to bond lengths pertaining to the structures resemble those of Kangas et al. [27]. All bond lengths are in Å.

Structure →		MR	hol7	octa23	octa123	hol7octa23(k)	octa1234(k)
Surface →		0.50	0.75	0.50	0.50	0.75	0.50
Sub-Surface →		0.00	0.00	0.50	0.75	0.50	1.00
Total →		0.50	0.75	1.00	1.25	1.25	1.50
L	Bond	d_{Cu-O}	d_{Cu-O}	d_{Cu-O}	d_{Cu-O}	d_{Cu-O}	d_{Cu-O}
1	Cu1 – O5	1.879	2.004	1.833	1.836	1.937 (1.929)	1.835 (1.856)
1	Cu2 – O5	1.855	1.857	1.844	1.894	1.877 (1.868)	1.889 (1.903)
2	Cu5 – O5	2.214	2.076	3.400	3.574	3.360 (3.343)	2.864 (3.628)
1	Cu1 – O7		1.833			1.860 (1.839)	
1	Cu2 – O7		2.346			2.241 (2.181)	
2	Cu7 – O7		2.018			2.234 (3.778)	
2	Cu5 – O1				2.011		2.092 (1.833)
2	Cu7 – O1				1.980		1.855 (2.630)
3	Cu1 – O1				2.036		2.200 (1.862)
2	Cu5 – O2			2.053	2.134	2.024 (2.046)	1.883 (2.176)
2	Cu7 – O2			2.039	2.015	1.939 (2.077)	2.712 (1.854)
2	Cu8 – O2			2.057	2.026	2.010 (2.047)	2.357 (2.293)
1	Cu2 – O2			2.005	1.989	2.189 (2.028)	1.978 (1.963)
2	Cu5 – O4						2.183 (1.878)
2	Cu8 – O4						1.827 (1.859)
3	Cu4 – O4						2.055 (2.344)

5.3 Work Function

The results of calculation for high coverage work functions are presented in this section. The same method used in previous chapters to calculate the work function is also used here. The results for high coverage work functions are provided in Table 5.2 with the changes in work function shown in Fig. 5.6. It follows from calculations that the value for the work function obtained for the 0.50 ML missing row structure is lower than that of the 0.50 ML $c(2\times2)$ structure. The decrease is in agreement with

previous results [90]. The trend follows as oxygen coverage increases, so does the work function. However, according to the results obtained for coverages between 1.00 ML and 1.50 ML, it is unclear what effect the surface reconstruction has on the work function. The average work function value for the high coverage structures, excluding the MR, hol7, and hol7octa23k cases is 5.72 eV with a standard deviation of 0.05. Note, that the same value for work function has been obtained for the octa23, octa123, and octa1234k structures, each of which correspond to different total coverages.

Table 5.2: Cu(001) Oxidized Surface Work Functions. The first column provides reference numbers relating each of the structures (second column) to Fig. 5.6. The third, fourth, and fifth columns give the total, surface, and sub-surface oxygen coverages in ML, respectively. The calculated work function values are provided in column six with the changes in the work function with respect to the clean copper surface given in column seven. The last three rows give the work function results for the three low index surfaces of copper oxide to use for comparison. Because of their oxide nature, the coverage for these three structures is uniform throughout the entirety of the bulk slab. All work function values are given in eV.

Ref	Structure	Total	Surface	Sub-Surface	Φ	$\Delta\Phi$
1	Clean Cu(001)	0.00	0.00	0.00	4.59	0.00
2	MR	0.50	0.50	0.00	4.71	0.12
3	hol7	0.75	0.75	0.00	4.79	0.20
4	oct23	1.00	0.50	0.50	5.75	1.16
5	oct123	1.25	0.50	0.75	5.75	1.16
6	hol7octa23	1.25	0.75	0.50	5.68	1.09
7	hol7octa23k	1.25	0.75	0.50	6.30	1.71
8	octa1234	1.50	0.50	1.00	5.65	1.06
9	octa1234k	1.50	0.50	1.00	5.75	1.16
10	$Cu_2O(100)$	uniform coverage			6.92	2.33
11	$Cu_2O(110)$	uniform coverage			5.94	1.35
12	$Cu_2O(111)$	uniform coverage			4.64	0.05

The structure that yielded the highest work function as compared to the other structures considered in this chapter was the hol7octa23k structure. One thing different about the hol7octa23 structure is the placement of the oxygen atom at the

surface and in the sub-surface regions in relation to the neighboring copper atoms. According to Fig. 5.4c, the octa23 oxygen atoms in the sub-surface region sit just above the copper atoms in layer 2. These copper atoms are nearly coplanar and their charges are nearly equal. As a result, the dipole moment attributed to the octa23 atoms points nearly perpendicular to the surface. For the surface atoms, there is a three to three ratio between copper and oxygen atoms. Additionally, the oxygen atoms, as a whole, are further away from the surface than are the Cu1, Cu2, and Cu3 atoms. This also contributes to a net maximum dipole moment that is directed perpendicular to the surface and in the same direction as the sub-surface dipole moment. Contributions of the sub-surface dipole moment to the net dipole moment are most likely one of the main causes for the high work function value obtained in calculation. This same argument can be applied to the other structures. For example, in the hol7octa23 structure, the Cu7 atom in the second layer is coplanar with the oxygen atom thereby producing an overall sub-surface dipole moment that has a much smaller z component. Also, the O7 atom sits below the plane containing the Cu1 atom and is now coplanar with the Cu2 atom. This induces an oppositely polarized dipole moment serves to partially cancel out the dipole moment arising from the interaction between the O5, O6, Cu2, and Cu3 atoms.

There are, of course, other factors that affect the value of the work function such as the amount by which the atoms in each layer are shifted in the z direction causing an overall surface relaxation whether it be inward or outward. Also the lateral shifting of atoms in surface and sub-surface layers can create regions of depleted charge which in turn provides a path for electrons to escape the surface more easily thereby reducing the work function.

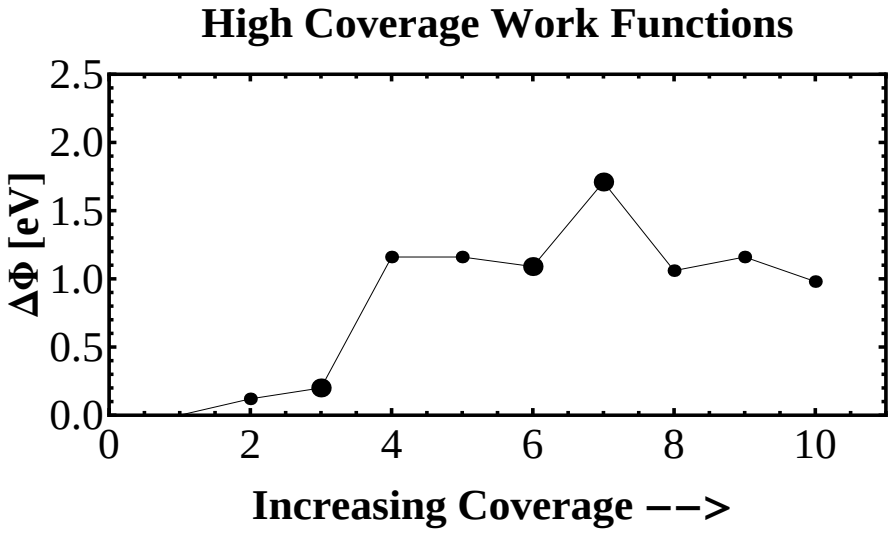

5.4 Density of States

Presented in this section are the results for the partial density of states. The calculated PDOS follows from the methods discussed in chapter 3 section 3.5. The plots for the PDOS are shown in Figs. 5.8, 5.9, and 5.10. In each figure, the PDOS pertaining to the p-state (dashed line) for a particular oxygen atom is plotted along with the d-state (solid lines) corresponding to those copper atoms that are the closest to the oxygen atom. To add clarification to the coloring in the PDOS plots a color key relating each PDOS curve to its constituent atom is provided in Fig. 5.7. Again, all energy measurements are taken with respect to the Fermi level represented by the thin vertical black line at $x = 0$.

From the results of the PDOS there appears to be two distinct bands as shown in Fig. 5.8 (a) pertaining to the MR structure. The first band, which is predominantly p-state in character, spans from -8 to about -4 eV while the second band, which is mostly d-state in character, spans from about -4 eV to the Fermi level. The shape of

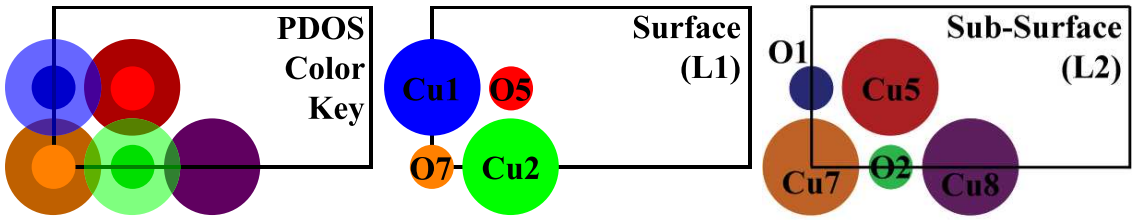

(a) (b) (c)

Figure 5.7: A (a) color key mapping the colors of the PDOS to their respective atoms is provided along with separate (b) surface and (c) sub-surface mappings. The large (small) circles represent copper (oxygen) atoms. Each atom in the surface layer (b) is the same color as (and brighter than) the atom directly beneath it in the sub-surface layer (c). The numbering of the color keys follows directly from 5.2.

the PDOS in the case of the MR structure is similar to that of the $c(2\times2)$ structure. The same bandwidth range is observed in Figs. 5.8 (b) and 5.8 (c) for the hol7 structure. In addition, two distinct peaks are also observed, one at -7.5 eV and the other at -5.5 eV, which indicate separate contributions from the original MR oxygen adatom, O5, and the now present O7 adatom.

Moving now to the 1.00 ML case, octa23, the band width narrows and shifts toward the Fermi level. For the O5 adatom, shown in Fig. 5.8 (d), the width of the first band which is again p-state dominated spans from about -6.5 eV to -3 eV with the second d-state band continuing up to the Fermi level. There are two major peaks in the first band lying at -5 and -3.5 eV with a minor peak at about -6 eV. The plot of O2 in Fig. 5.8 (e) again shows two distinct bands. The first p-state band ranges from about -6.5 eV to -4.5 eV while the second d-state band ranges from about -4.5 eV up to the Fermi level. At -5.0 eV the O2 adatom has its greatest intensity with a secondary peak at approximately -6.0 eV

The PDOS results for the 1.25 ML cases are shown in Figs. 5.9 (a - i). For the octa123 structure, the same bandwidth and shape of the PDOS curves that were

observed for the O5 adatom in the octa23 case are also observed here. However the contributions to the PDOS arising from the O2 sub-surface adatom and its neighboring copper atoms as shown in Fig. 5.9 (c) are not as distinct as they were in the octa23 case. In particular, the oxygen p-state bandwidth has broadened out to about 3 eV which is also accompanied by a decrease in peak intensity. As for the copper d-states, the smooth overlap between each copper d-state as observed in Fig. 5.9 (c), is no longer present. The results of the PDOS from the O1 adatom and neighboring copper atoms shown in Fig. 5.9 (b) are similar to the O2 adatom results as far as bandwidth ranges and overlap are concerned. From the results presented thus far, the changes in shape and shifting of the PDOS can be most likely attributed to two things: First, the range in bond lengths between the sub-surface oxygen adatoms and each of the neighboring copper atoms as compared to the octa23 case shown in Table 5.1 increases. Second, the sub-surface layer L_2 is no longer well defined as some of the copper atoms and oxygen adatoms have been displaced due to reconstruction along the z directions as shown in Fig. 5.4 (a).

For the hol7octa23 and hol7octa23k structures, there isn't a well defined oxygen p-state band for either of the surface oxygen atoms shown in Figs. 5.9 (d), (e), (g), and (h). However, the p-state band is noticeable for the sub-surface oxygen atoms shown in Figs. 5.9 (f) and (i). Also, the shape of the PDOS is in close comparison to Fig. 5.8 (e) which suggests that there is a stronger correlation between copper atoms neighboring sub-surface oxygen adatoms than there is to copper atoms neighboring surface oxygen adatoms.

The final PDOS results for the two 1.50 ML cases, octa1234 and octa1234k are shown in Figs. 5.10 (a - h). The p-state and d-state bandwidths corresponding to the surface states shown in Figs. 5.10 (a) and 5.10 (e) are nearly identical to those observed in Figs. 5.8 (d) and 5.9 (a). The sub-surface p-state bands are shifted

slightly to the left, away from the Fermi level covering a range between -8 to -5 eV shown in Figs. 5.10 (b) and 5.10 (f). The intensity of all p-state DOS peaks in Figs. 5.10 (b), 5.10 (c), and 5.10 (d) are higher and more narrow as compared to the corresponding p-state DOS peaks shown in Figs. 5.10 (f), 5.10 (g), and 5.10 (h).

The intensity of the oxygen PDOS peak corresponding to -7.5 eV in Fig. 5.10 (h) is higher than the intensity of the PDOS peak at -6.25 eV. This is due to contributions from the s-states (not shown) of the neighboring copper atoms. This is also observed in Figs. 5.10 (b), 5.10 (f) for the small PDOS peaks located at -7.5 eV. Upon further investigation it was found that the other structures considered in this chapter follow the same trend in that the s-states contribute mostly to the low energy PDOS peaks. Lastly, the decrease in d-state overlap corresponding to sub-surface copper atoms observed in the 1.25 ML case of the octa123 structure is also observed in both 1.50 ML cases.

In summary, these results further prove that there is a correlation between density of states and the (1) displacement of atoms along the line perpendicular to the surface, and the (2) bond length between oxygen adatoms and nearest neighbor copper atoms.

5.5 Difference Electron Density and Deformation Density

In this section, the results for the deformation and difference electron density are presented. The same techniques that were used in the previous chapter regarding the deformation density are used here. For the difference electron density, the calculations performed for $\rho^{O}(\mathbf{r})$ at and above 1.00 ML coverage failed to converge due to the increased number of oxygen atoms in the cell. Thus, a slightly different approach was considered in this thesis as an attempt to work around this problem. Instead of isolating all the oxygen atoms from the original slab, only the surface atoms were

extracted, leaving behind the sub-surface atoms to be calculated with the rest of the copper atoms. This may be expressed as,

$$\rho^{\Delta}(\mathbf{r}) = \rho^{Cu+O}(\mathbf{r}) - \rho^{Cu+O_{Sub}}(\mathbf{r}) - \rho^{O_{Surf}}(\mathbf{r}), \tag{5.1}$$

where $\rho^{Cu+O_{Sub}}(\mathbf{r})$ is the substrate density with surface atoms removed and $\rho^{O_{Surf}}(\mathbf{r})$ is the density corresponding to the removed surface atoms.

For each structure considered in this chapter, deformation density and difference electron density plots representing each of the four symmetric vertical cut planes, are presented. For example, Fig. 5.15 shows the deformation density through the Y50 cut plane. This plane is located along the y axis at a position equal to 50% of the y direction width of the slab, hence the name Y50. This plane, which corresponds to the blue lines in Fig. 5.11a and 5.11c, is represented by corresponding a blue boarder around the plots in Fig. 5.15.

The same observations regarding the deformation and difference electron density that were discussed in Section 4.6 and 4.6 are also observed here. There is an obvious charge accumulation in the vicinity of the oxygen atoms and a charge depletion occurring just outside the copper atoms closest to the surface. This further suggests that the charge transfer effects observed, take place primarily between the oxygen atom and the copper atoms in the first surface layer. The behavior of the difference electron density observed in Figs. 5.16 (a - h), 5.17 (a - h), 5.18 (a - h), and 5.19 (a - h) will also be explored in future studies.

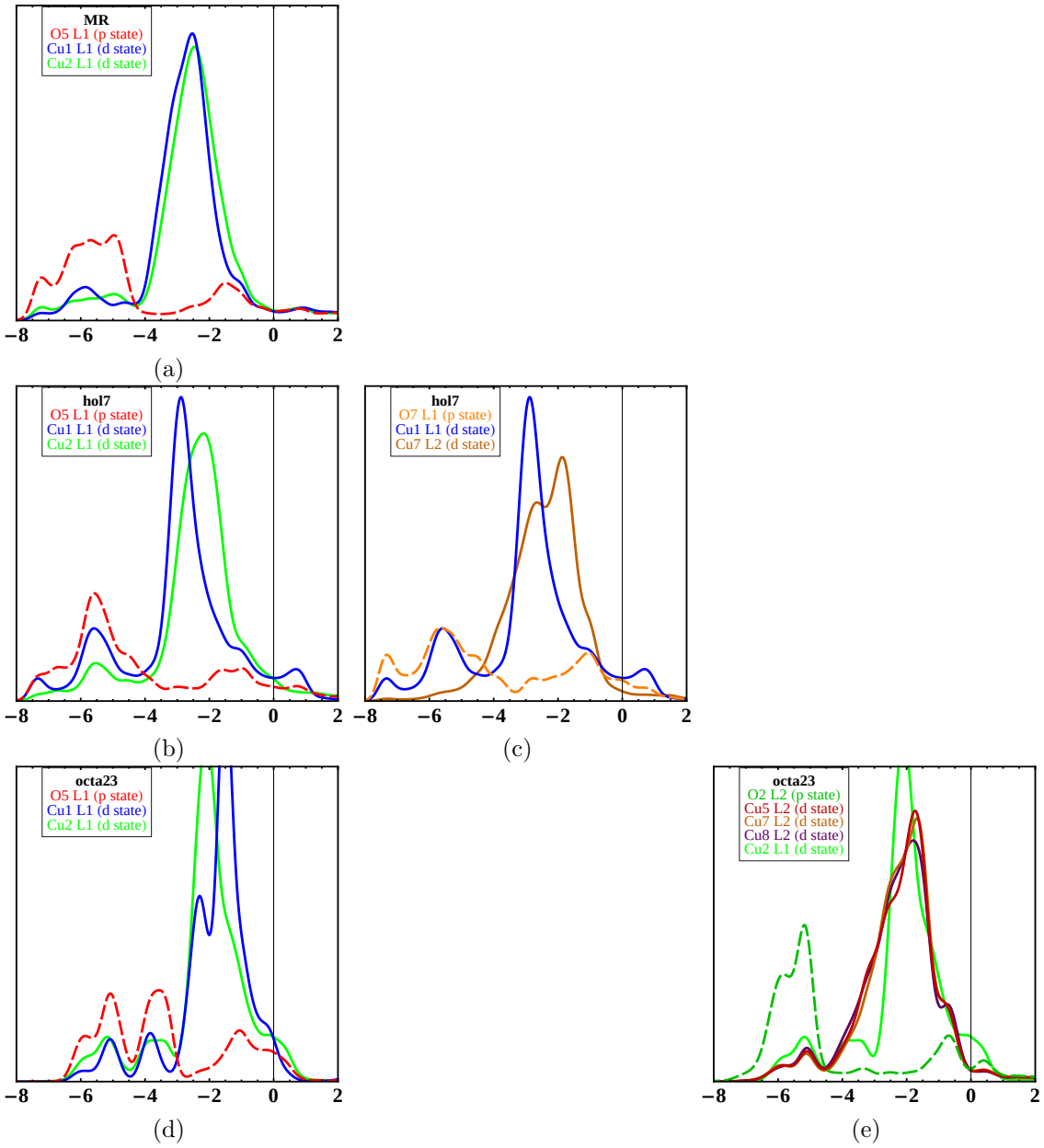

Figure 5.8: High coverage ($\Theta \leq 1.00$ ML) PDOS for the (a) Hol5 oxygen adatom in the MR structure, the (b) Hol5 and (c) Hol7 oxygen adatoms in the hol7 structure and the (d) Hol5 and (e) Octa2 oxygen adatoms in the octa23 structure. Plots are aligned horizontally according to the structure they represent and vertically according to the oxygen adatom. The color mapping is shown in Fig. 5.7. The units of the X axis are in eV while the units of the Y axis are arbitrary units. The Fermi level is shown as a thin black vertical line at $x = 0$.

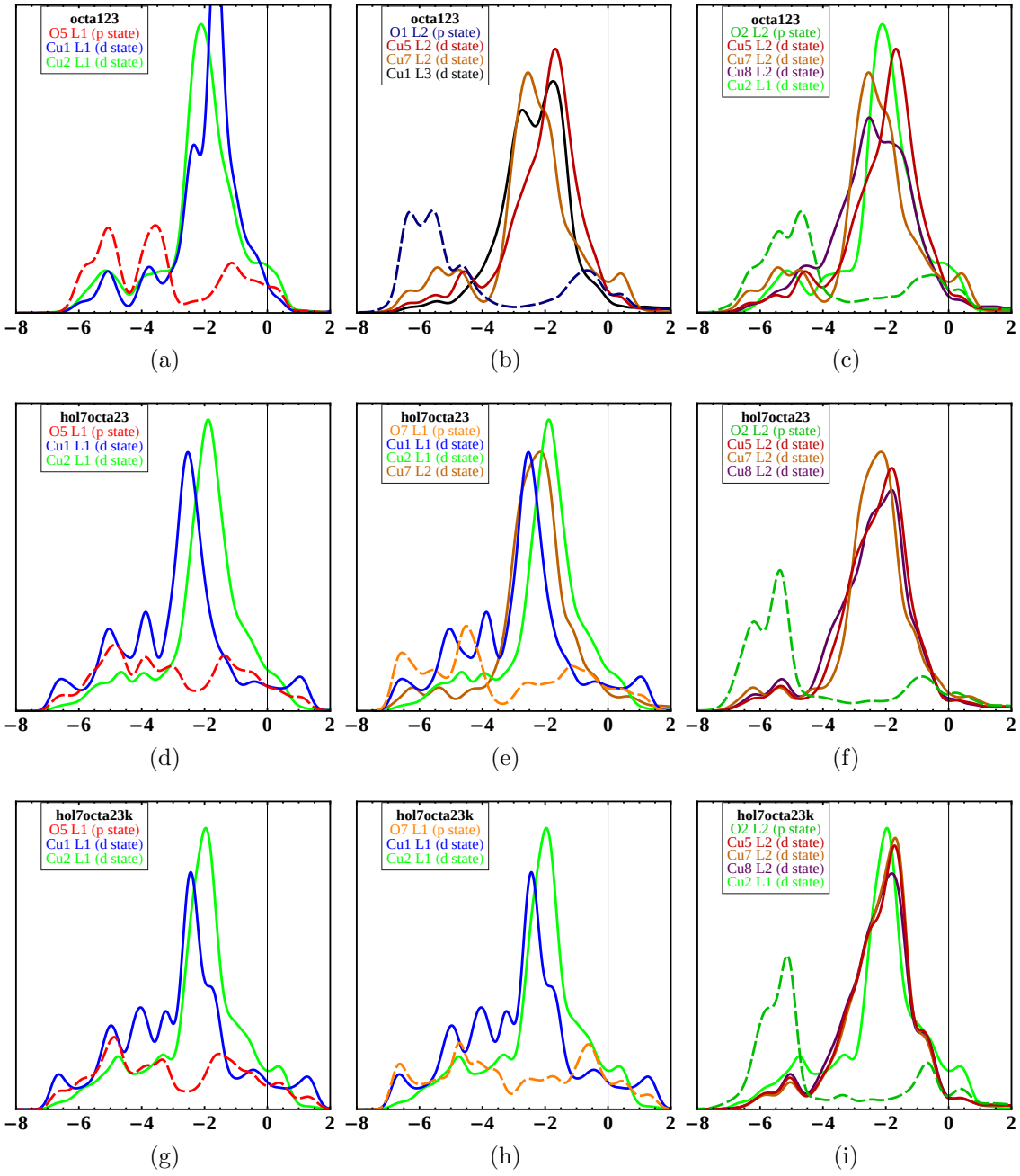

Figure 5.9: High coverage ($\Theta = 1.25$ ML) PDOS for the (a) Hol5, (b) Octa1, and (c) Octa2 oxygen adatoms in the octa123 structure, the (d) Hol5, (e) Hol7, and (f) Octa2 oxygen adatoms in the hol7octa23 structure, and the (g) Hol5, (h) Hol7, and (i) Octa2 oxygen adatoms in the hol7octa23k structure. Refer to Fig. 5.10 for further details.

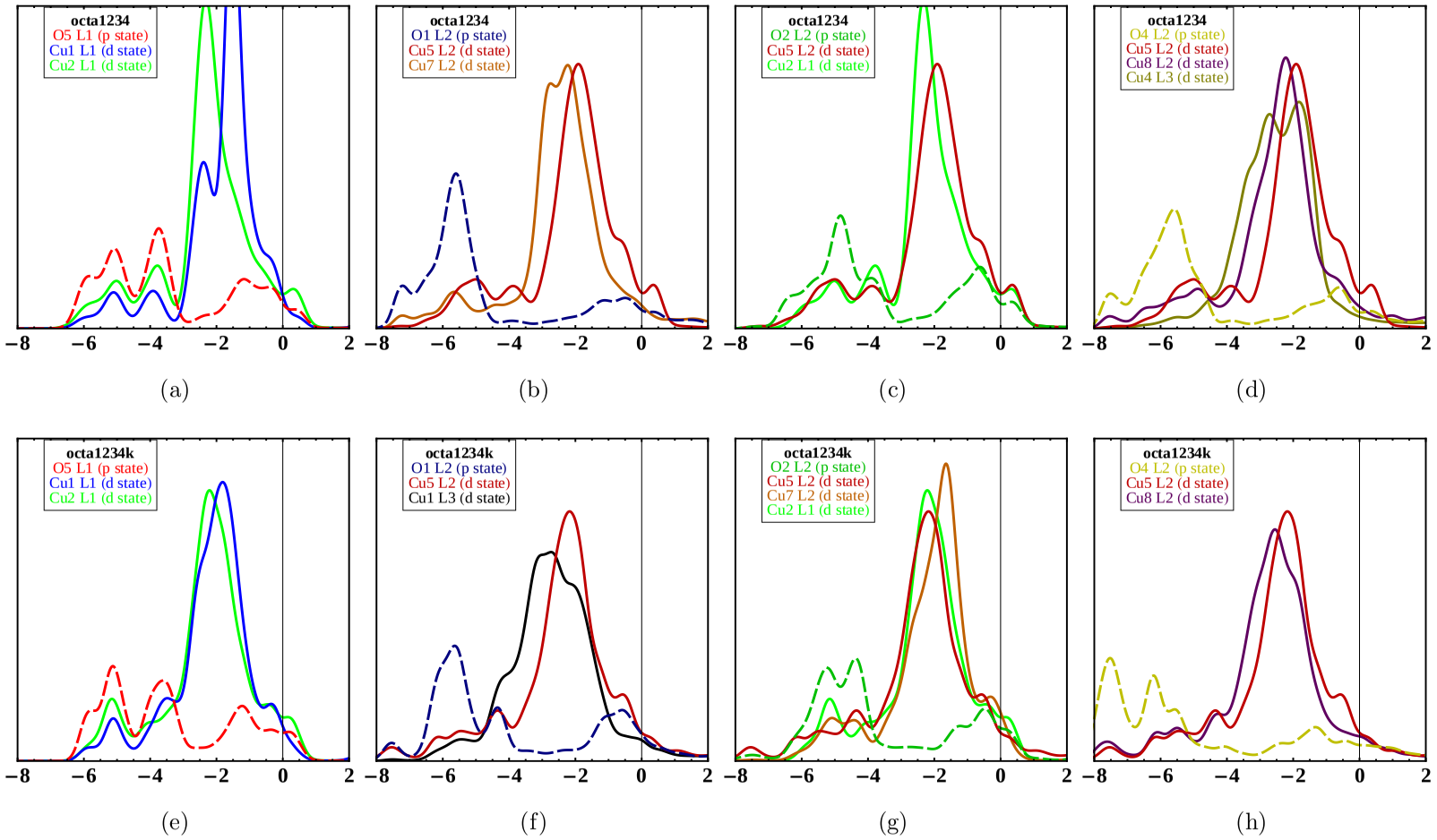

Figure 5.10: High coverage ($\Theta = 1.50$ ML) PDOS for the (a) Hol5, (b) Octa1, (c) Octa2, and (d) Octa4 oxygen adatoms in the octa1234 structure and the (e) Hol5, (f) Octa1, (g) Octa2, and (h) Octa4 oxygen adatoms in the octa1234k structure. Refer to Fig. 5.10 for further details.

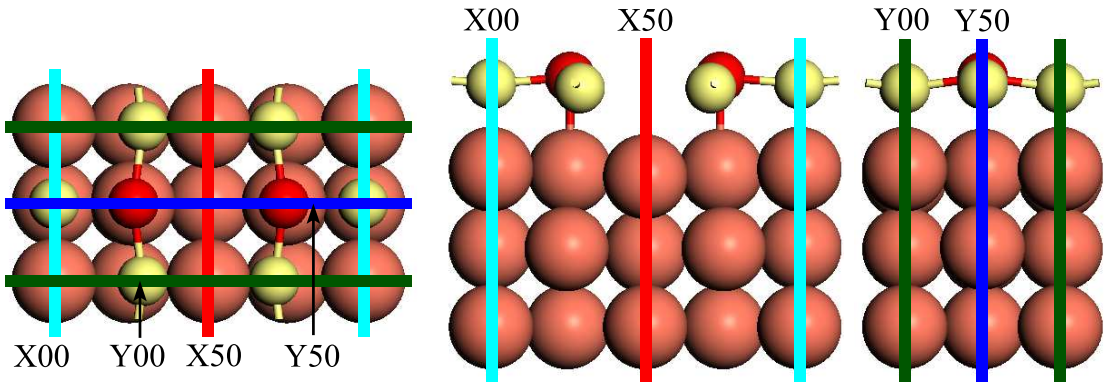

Figure 5.11: Contour plane schemes for the MR Structure as viewed from (a) the top, (b) the [010] direction and (c) the [100] direction. The teal and red lines represent cut planes normal to the x axis at 0.00 and 0.50 fractional units, respectively. The green and blue lines represent cut planes normal to the y axis at 0.00 and 0.50 fractional units, respectively.

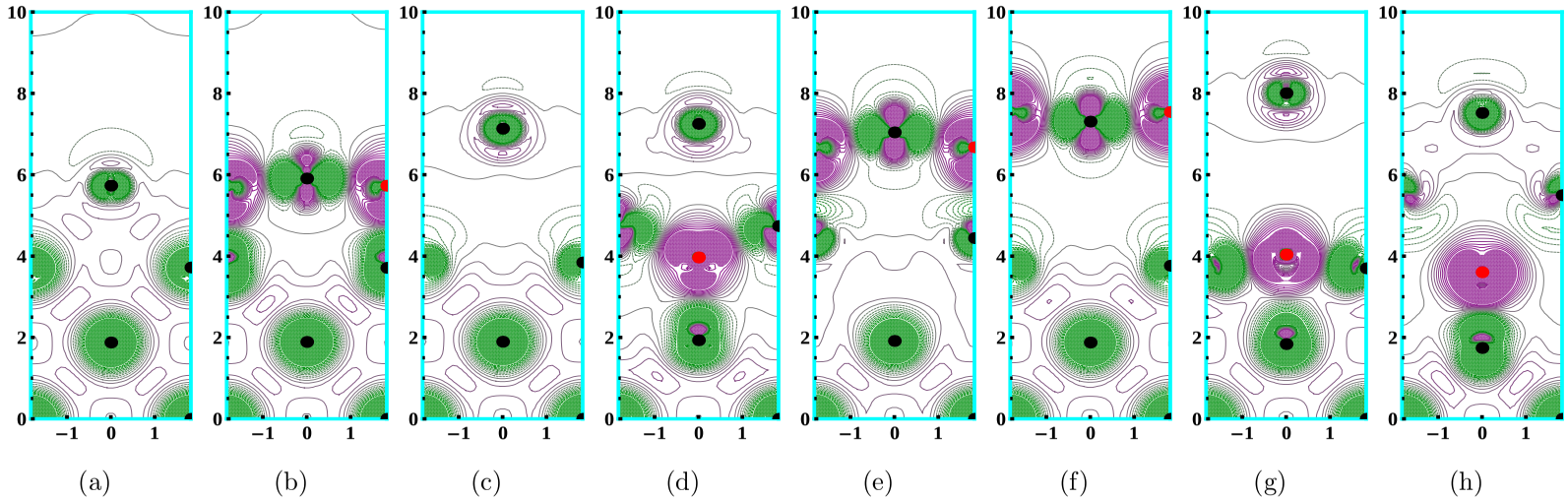

Figure 5.12: High coverage deformation density plots in the X00 (teal border) plane for the (a) MR, (b) hol7, (c) octa23, (d) octa123, (e) hol7octa23, (f) hol7octa23k, (h) octa1234, and (i) octa1234k structures. The centers of the copper/oxygen atoms are colored black/red. Solid (violet) contours represent regions of charge accumulation, while dashed (green) lines represent regions of charge depletion. Contours lines are drawn at $2.5\times10^{-3}\,\mathrm{elec/\AA^3}$ intervals ranging from $\pm0.1\,\mathrm{elec/\AA^3}$. The y and z axes are in units of Å with $z = 0$ representing the center of the slab.

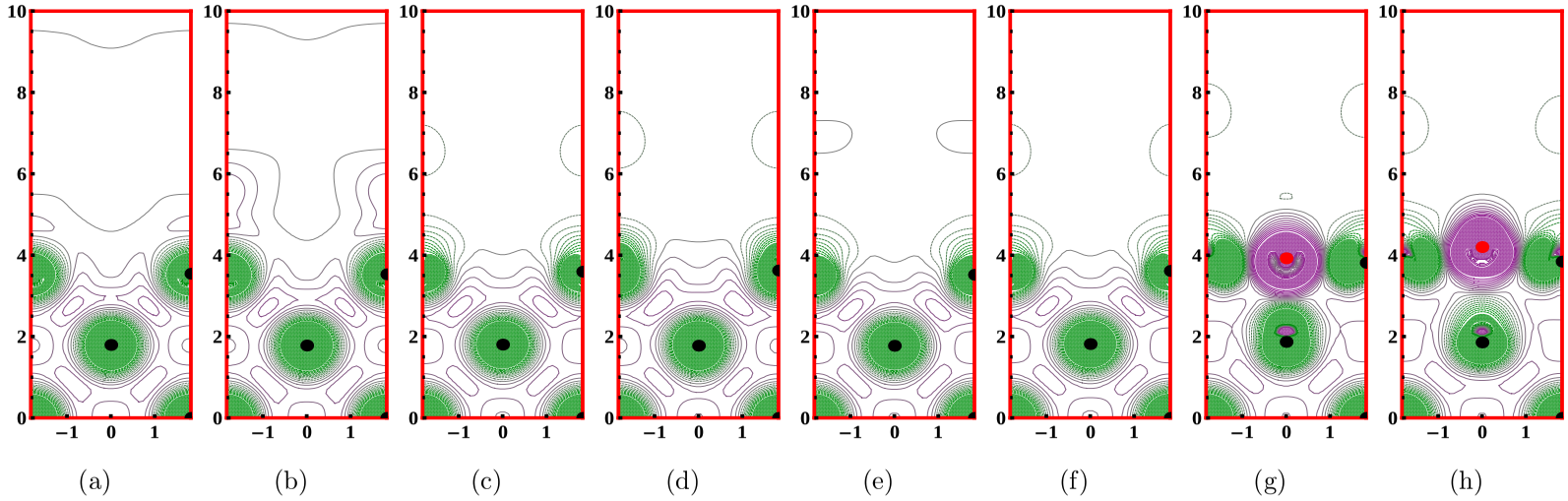

Figure 5.13: High coverage deformation density plots in the X50 (red border) plane for the (a) MR, (b) hol7, (c) octa23, (d) octa123, (e) hol7octa23, (f) hol7octa23k, (h) octa1234, and (i) octa1234k structures. The y and z axes are in units of Å. Refer to Fig. 5.12 for further details.

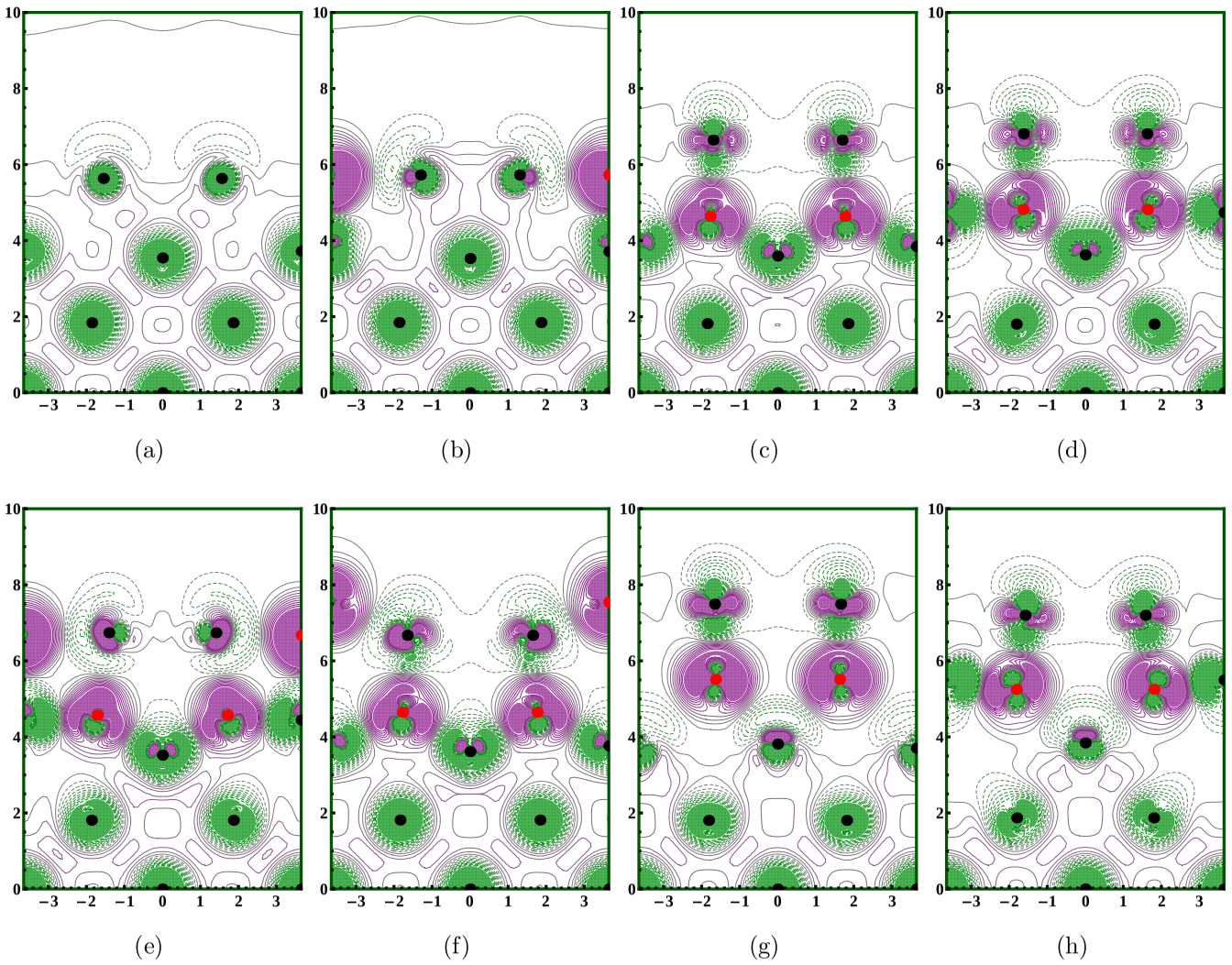

Figure 5.14: High coverage deformation density plots in the Y00 (green border) plane for the (a) MR, (b) hol7, (c) octa23, (d) octa123, (e) hol7octa23, (f) hol7octa23k, (h) octa1234, and (i) octa1234k structures. The x and z axes are in units of Å. Refer to Fig. 5.12 for further details.

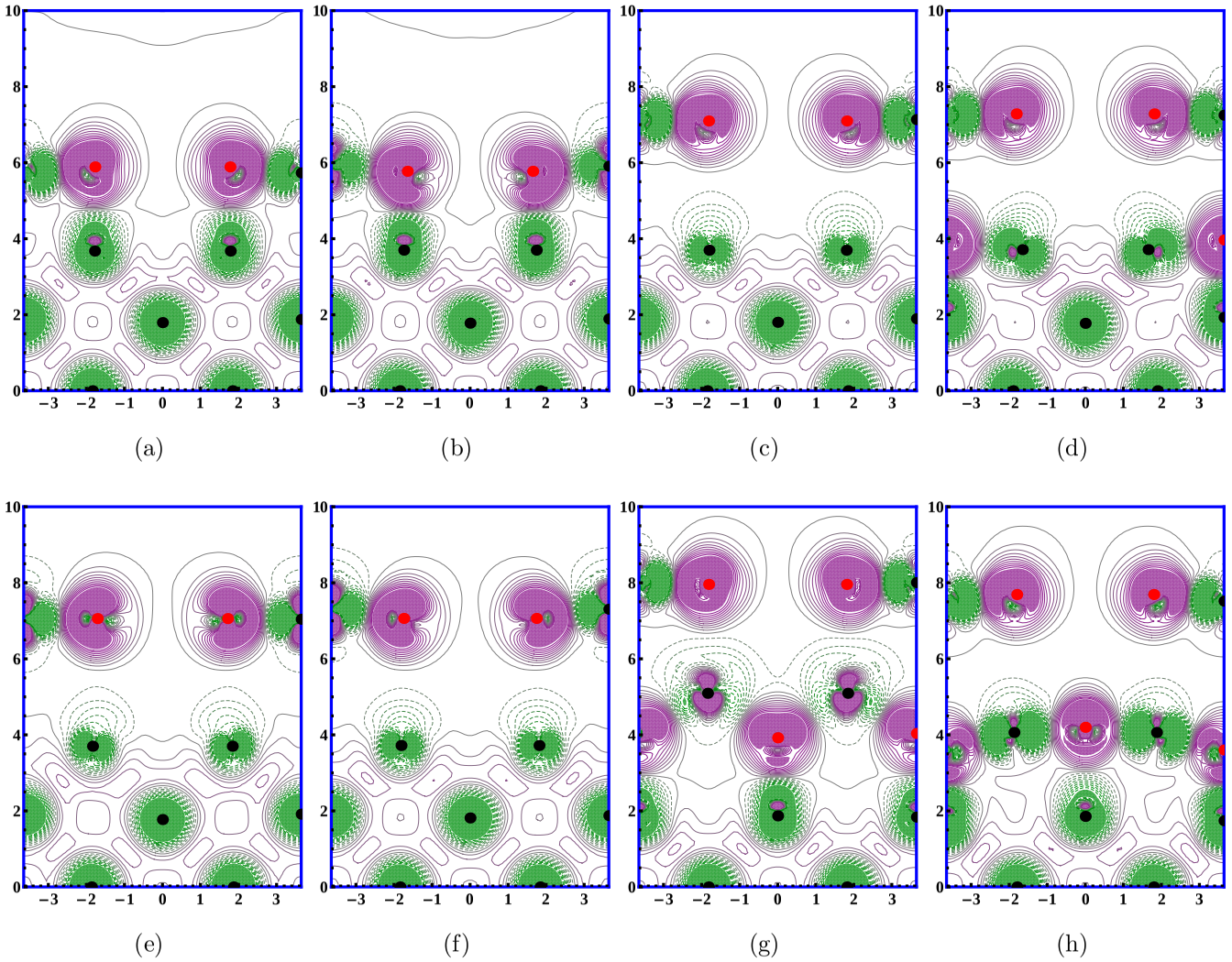

Figure 5.15: High coverage deformation density plots in the Y50 (blue border) plane for the (a) MR, (b) hol7, (c) octa23, (d) octa123, (e) hol7octa23, (f) hol7octa23k, (h) octa1234, and (i) octa1234k structures. The x and z axes are in units of Å. Refer to Fig. 5.12 for further details.

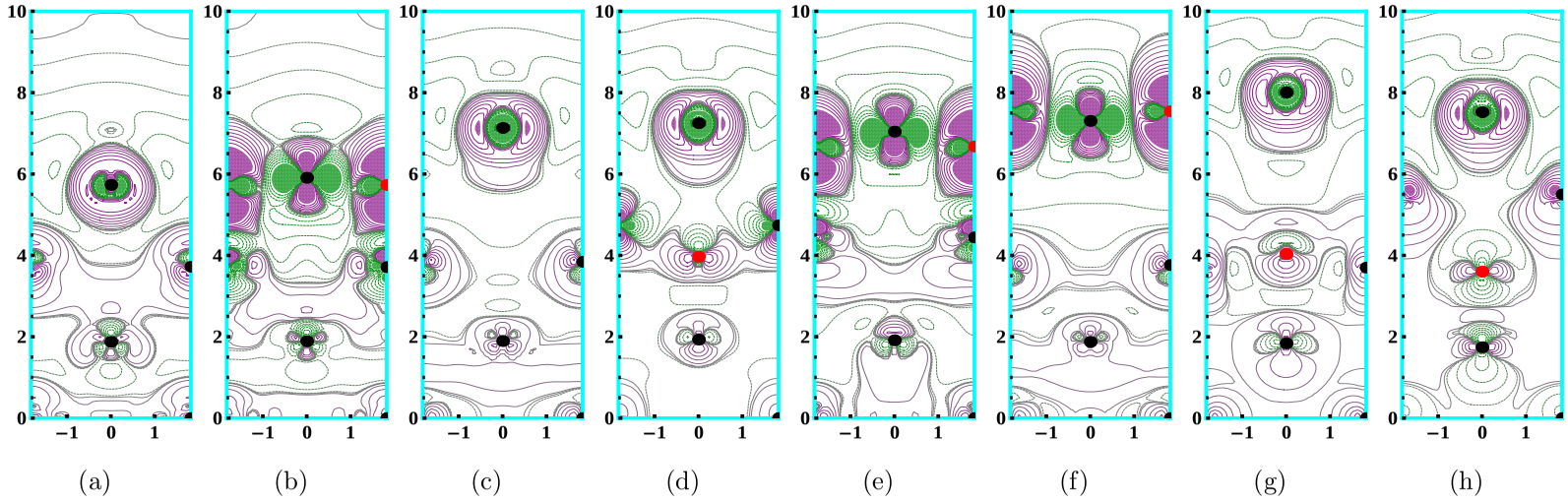

Figure 5.16: High coverage difference density plots in the X00 (teal border) plane for the (a) MR, (b) hol7, (c) octa23, (d) octa123, (e) hol7octa23, (f) hol7octa23k, (h) octa1234, and (i) octa1234k structures. The centers of the copper/oxygen atoms are colored black/red. Solid (violet) contours represent regions of charge accumulation, while dashed (green) lines represent regions of charge depletion. Contours range from $\pm 0.1\,\mathrm{elec/\AA^3}$ and are separated by a factor of ρ^3. The y and z axes are in units of Å where the plane corresponding to $z = 0$ represents the center of the slab.

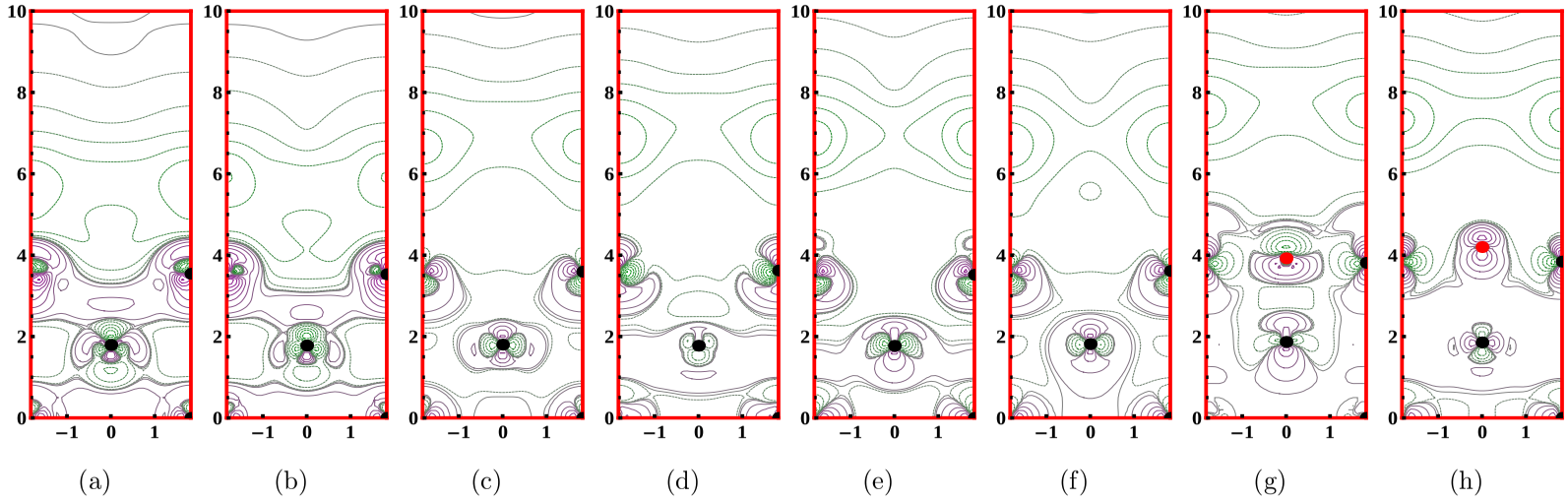

Figure 5.17: High coverage difference density plots in the X50 (red border) plane for the (a) MR, (b) hol7, (c) octa23, (d) octa123, (e) hol7octa23, (f) hol7octa23k, (h) octa1234, and (i) octa1234k structures. The y and z axes are in units of Å. Refer to Fig. 5.16 for further details.

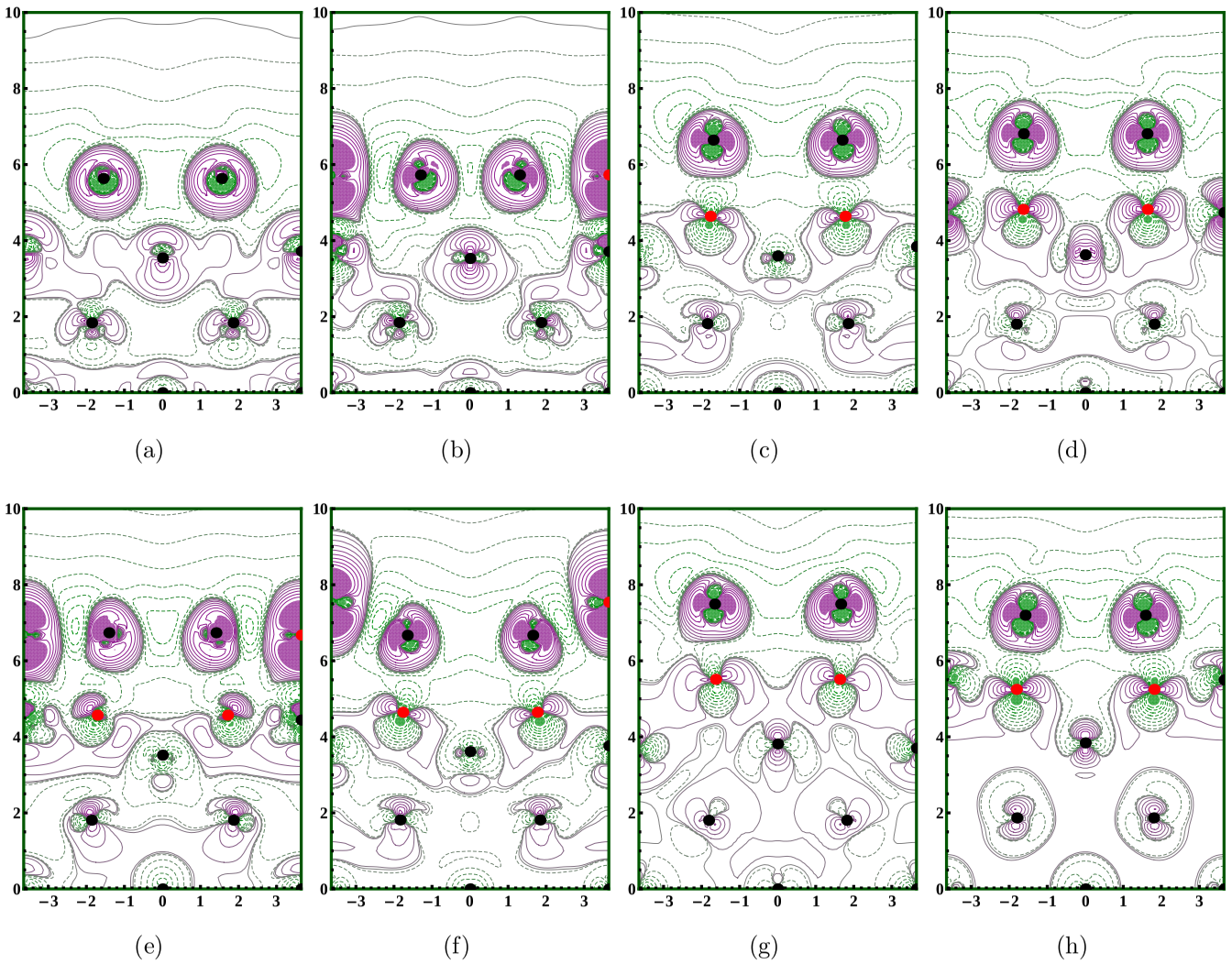

Figure 5.18: High coverage difference density plots in the Y00 (green border) plane for the (a) MR, (b) hol7, (c) octa23, (d) octa123, (e) hol7octa23, (f) hol7octa23k, (h) octa1234, and (i) octa1234k structures. The x and z axes are in units of Å. Refer to Fig. 5.16 for further details.

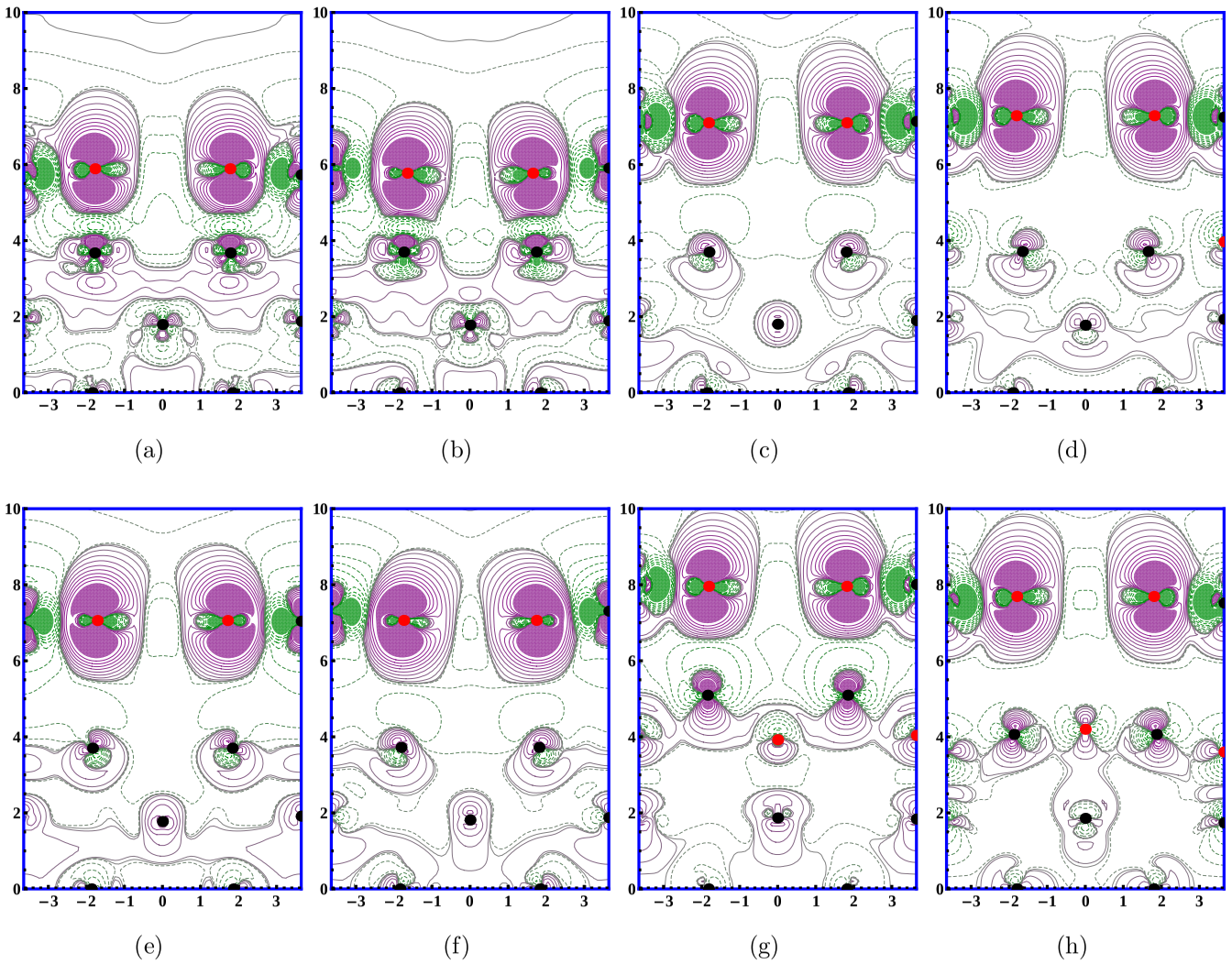

Figure 5.19: High coverage difference density plots in the Y50 (blue border) plane for the (a) MR, (b) hol7, (c) octa23, (d) octa123, (e) hol7octa23, (f) hol7octa23k, (h) octa1234, and (i) octa1234k structures. The x and z axes are in units of Å. Refer to Fig. 5.16 for further details.

CHAPTER 6

CONCLUSION

In this thesis, first principles studies of electronic properties of clean Cu(001), Cu(110), and Cu(111) surfaces, as well as oxidized Cu(001) surfaces have been conducted using density functional theory as implemented in the DMol3 computer code.

6.1 Summary of Results

From the results obtained in Chapter 3 for clean Cu(001), Cu(110), and Cu(111) surfaces it was shown that both the work function and interlayer relaxations between copper layers for all the studied surfaces were in better agreement with experimental data than the previously reported theoretical values. It has been shown also that the calculated total and partial density of states for pure Cu(001) agree well with previous theoretical results.

It follows from the results obtained in Chapter 4 for the case of low coverage oxygen adsorption on the Cu(001) surface that the bond length between the oxygen adatom and its nearest neighbor copper atom as well as the height of the oxygen atom above the copper surface, agree extremely well with previously obtained results for the 0.25 and 0.50 ML coverages. The new results obtained for the 0.11 ML coverage follow the correct trend. The results for interlayer relaxations were also calculated for low oxygen coverages. It follows from these results that the average interlayer spacing for 0.11 and 0.25 coverages are about the same. However, a significant expansion of the surface layer toward the vacuum has been observed for the 0.50 ML coverage. It has been found from comparing the interlayer spacings between the relaxed and

unrelaxed structures, that the values pertaining to the unrelaxed structure were much lower (closer to zero) than for the relaxed structure. This suggests that the coordinates of the unrelaxed structure provide a better initial guess to the geometry of the substrate/adsorbate system.

The effect of oxygen adsorption on the electron work function has been studied also for three oxidized low coverage structures on Cu(001). It follows from the results of these studies, that the work function increases with the coverage up to 0.25 ML followed by a further increase up to 0.50 ML coverage. These computed values for the work function follow the trend that work function is directly proportional to oxygen coverage. In addition, the computed PDOS for low oxygen coverages have been found to agree well with the results obtained in previous studies.

The computed low coverage deformation and difference electron density plots suggest that charge redistribution at the surface takes place at all studied low coverage oxygen structures on Cu(001). It follows from these plots that the charge accumulation surrounding the adsorbed oxygen atom at the surface is a direct result of charge transfer effects between the surface adsorbed oxygen atom and the Cu(001) substrate. As a result, the increase in the work function has been observed with the increase of oxygen coverage.

The effects of oxidation of Cu(001) on electronic properties have been studied also for high oxygen coverage structures. Two separate surface atomic structure configurations corresponding to each of the 1.25 ML and 1.50 ML oxygen coverages have been found to have stable geometries. Values for the bond length between oxygen atoms and nearest neighbor copper atoms for all optimized structures were also calculated.

The electron work function has been calculated for all high coverage adsorbed oxygen structures on the Cu(001) taking into account reconstruction of the surface.

A decrease in work function has been observed when changing from the 0.50 ML $c(2\times2)$ phase to the 0.50 ML missing row phase. This trend was also seen in previous studies. It has been found that as oxygen coverage increases from the 0.50 ML missing row structure to the 1.00 ML octa23 structure the work function increases. For coverages between 1.00 ML and 1.50 ML, no noticeable change has been observed in the work function. The largest calculated value for the work function (other than for $Cu_2O(100)$) of 6.3 eV has been obtained for the hol7octa23k phase which is probably mostly due to the largest dipole induced in the surface region due to charge transfer effects.

The results pertaining to the calculation of partial density of states have also been obtained for high oxygen coverages. The plots corresponding to the PDOS for the case of all oxygen p-states and all nearest neighbor copper d-states have been constructed and explored. A correlation between the Cu - O bond length and p-state/d-state overlap has been found from these studies. It follows from the results obtained for high adsorbate oxygen coverages on Cu(001) surface that for coverages between 1.00 ML and 1.50 ML the surface and sub-surface layers expand outward into the vacuum. The shifting of the DOS toward the Fermi level for atoms in the surface state has been observed also when the top layers expand.

6.2 Additional Notes

All DMol3 calculations performed in this thesis were done using the RIR8002 computer cluster located at the High Performance Computing center which is maintained by the University of Texas at Arlington. DMol3 is part of the Materials Studio v4.4 software package developed by Accelrys Inc. Materials studio provides a nice interface for constructing, modifying, and visualizing three dimensional atomistic structures. Many software packages were used to supplement analysis of the results

obtained from DMol3 calculations. The Atomic profile plots found throughout this thesis were first generated by Materials Studio then converted into EPS format using Adobe Photoshop. All other plots including PDOS and density contour plots were generated using Mathematica v7.0. Unfortunately, the results of DMol3 calculations could not be ported directly into Mathematica. As a result, the software data analysis tool, IDL, was used to import, preprocess and export the results in a format suitable for Mathematica. This document was typeset with LaTeX 2_ε on May 4, 2009.

APPENDIX A

UNIT CELL CALCULATIONS

Before constructing vacuum slabs to be used in surface calculations it is necessary to find an acceptable value of the lattice constant for the substrate unit cell such that the total energy is minimized. The known experimental lattice constants used by default in Materials Studio, unfortunately do not always yield a configuration of minimum total energy in theoretical computational models due to the wide range of input parameters available, not only in DMol3 but in all DFT related codes. Two of these such input parameters, namely, the choice of core electron treatment and real-space cutoff were explored to help determine a suitable value for the lattice constant appropriate for the present study.

A.1 Orbital Cutoff

When performing numerical integrations, the charge density must be integrated over all space. The electron wave functions used to determine this charge density extend to infinity but converge rapidly within a few angstroms away from the core. Thus all space not in the immediate vicinity of the atom may, in principle, be excluded from calculations without significantly biasing the final results. This is accomplished by imposing an orbital cutoff parameter to the electron wave functions. The cutoff parameter limits the range to which the orbitals radially extend out from the nucleus. A smaller cutoff value results in a lower computational cost, however a larger cutoff improves the accuracy of calculation. Thus it is important to find the smallest value of cutoff that still gives accurate results.

A.2 Core Treatment

As stated before, each electron wave function dies rapidly as it extends out from the nucleus. The outermost valence orbitals extend the farthest away from the core

whereas the innermost orbitals are, for the most part, tightly bound to the core thus giving little contribution to the bonding of neighboring atoms. One way to achieve faster convergence is to neglect any contribution from these core electrons and instead account for them by adding an additional pseudopotential term to the exchange correlation potential. In the pseudopotential approach the nuclei and core electrons are treated as a single ion leaving only the valence electrons to be included in the calculation of $V_H(\mathbf{r})$. This is unlike the all-electron method where all of the electron orbitals in the Hartree potential are computed. All-electron methods are theoretically more accurate than pseudopotential methods, however they are also more computationally expensive. Heaver atoms are affected more by the use of pseudopotentials due to the increased number of core states but calculations with medium sized atoms, such as copper, can also benefit from the use of pseudopotentials.

Relativistic core treatments are also available. They cost more computationally but provide a more accurate treatment of electrons especially in heaver atoms. According to the literature, relativistic core treatments need not be included unless dealing with atoms heaver than Krypton (Z=36) [91]. With heavier elements, relativistic effects become important in the core electrons. In DMol3, The All-Electron Relativistic (VPSR) option not only includes all electrons explicitly, but also introduces scalar relativistic effects in the core electrons. [92, 93] This option yields the highest accuracy in calculations, but also the highest computational cost. An alternative to VPSR calculations is to use DFT semi-core pseudopotentials (DSPP) [94]. DSPP's replace the effects of core electrons with a simple single pseudopotential term but with some degree of relativistic effects included. The DSPP's can be very useful approximations for heavier elements.

Since this thesis involves computation of crystals containing only Copper ($Z = 29$) and Oxygen ($Z = 8$) atoms, one might choose a non-relativistic core treatment

for the study. However, some authors include relativistic effects in their calculations when dealing with atoms where $Z < 36$ [25, 28, 95]. For this reason, both cases will be investigated.

A.3 Results

In order to find an appropriate value for the lattice parameter we must first optimize the unit cell. To do this, we vary the volume of the unit cell and calculate the total energy of the system. We then plot the total energies as a function of volume and use the Murnaghan equation of state to fit the data [96],

$$E(V) = E_0 + \frac{B_0 V}{B_0'}\left(\frac{(V_0/V)^{B_0'}}{B_0' - 1} + 1\right) - \frac{B_0 V_0}{B_0' - 1} \tag{A.1}$$

where E, V, and B are the energy, volume, and bulk modulus respectively. The subscript zero denotes the equilibrium state. The bulk modulus, B_0, is related to the curvature of the total energy, $E(V)$, close to the equilibrium volume, V_0,

$$B_0 = -V\left.\frac{\partial^2 E(V)}{\partial V^2}\right|_{V=V_0}. \tag{A.2}$$

The pressure derivative of the bulk modulus, B_0', is calculated at equilibrium,

$$B_0' = \left.\frac{\partial B(p)}{\partial p}\right|_{p=0}, \tag{A.3}$$

and is found to change little with changing pressure. The resulting fit from A.1 gives the equilibrium volume which is used to determine the lattice constant $a = \sqrt[3]{V_0}$.

To find the equilibrium lattice constant we use Eq. A.1. The minimum values for the curves plotted in Fig. A.1 with their respective energy values are listed in Table A.1. The results for the lattice parameter are accurate to two decimal places with only a slight variation in the third decimal place. For the three core cases considered, changes in the lattice parameter with respect to increased cutoff radius

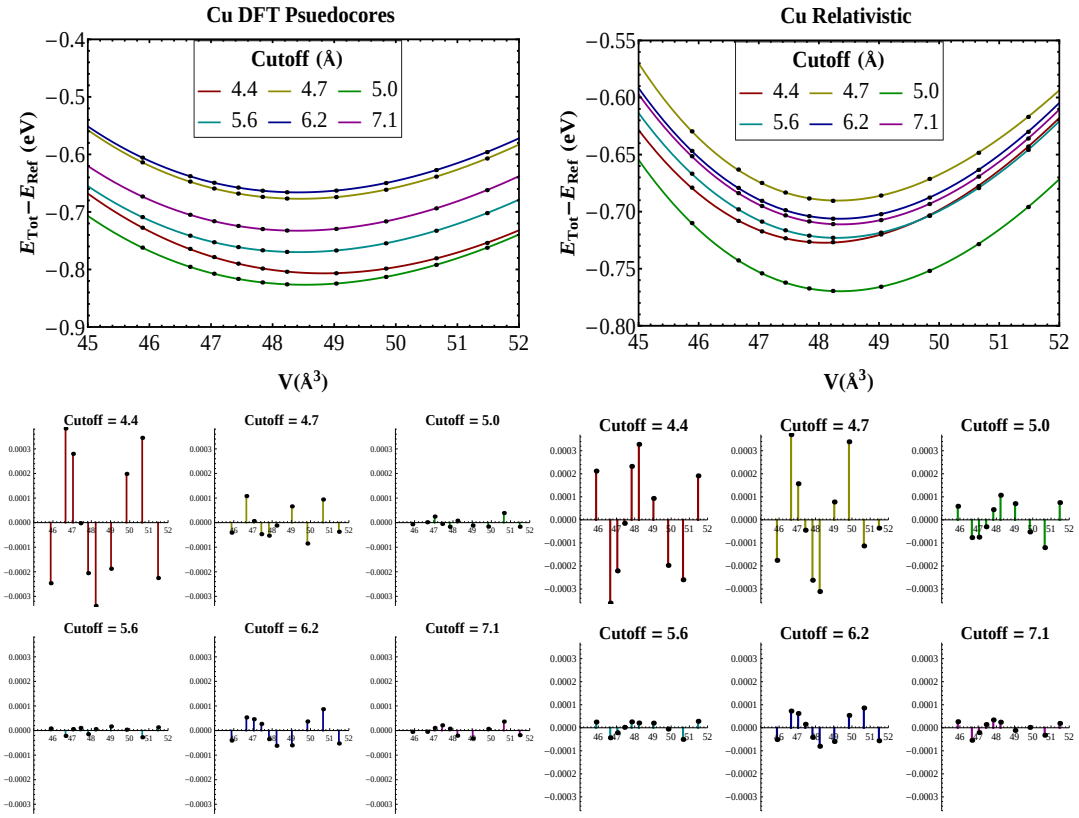

Figure A.1: Bulk copper total energy vs volume. The values of the total energy calculated with various orbital cutoff values have been fitted to Eq. A.1 The energy values plotted against the Y axis for the all-electron and pseudopotential cases are scaled by $E_{Ref} = -179397$ and $E_{Ref} = -24222$, respectively. The six smaller plots below each large plot show the residuals to each cutoff fit.

appear to decrease and mildly oscillate. The average lattice constants obtained from Eq. A.1 for all-electron non-relativistic, all-electron relativistic, and psuedopotential relativistic core treatments are 3.68, 3.64, and 3.65 Å, respectively. Both relativistic core treatments gave better results than the non-relativistic case with comparison to the experimental lattice constant 3.615 Å.

Similar to the results found for copper were the results of calculation for Cu_2O. For a given core treatment, the changes in the Cu_2O lattice parameter oscillated, but changed little with respect to increased cutoff radius. The average lattice constants

Table A.1: Minimized bulk properties for copper.

Cu	All-Electron			Pseudopotential		
cutoff(Å)	a(Å)	B_0(GPa)	Time (m)	a(Å)	B_0(GPa)	Time (m)
4.4	3.638	133.8	16.54	3.656	129.1	7.86
4.7	3.643	136.1	25.66	3.646	133.7	11.34
5.0	3.644	134.3	35.24	3.648	128.6	15.56
5.6	3.642	134.1	64.20	3.646	128.9	30.66
6.2	3.644	136.4	62.82	3.645	130.9	77.41
7.1	3.644	135.3	155.68	3.645	130.3	130.87

obtained were 4.35, 4.32, and 4.32 Å, respectively. Again, Both relativistic core treatments gave better results as compared to experiment, 4.27 Å.

From this, it was concluded that an all-electron non-relativistic core treatment may not be well suited for the present study. Thus, the tables and plots showing the results using the all-electron non-relativistic core treatment have been omitted. From this point on, when referring to the core treatments it should be assumed that relativistic effects are included.

Table A.2: Minimized bulk properties for Cu_2O.

Cu_2O	All-Electron			Pseudopotential		
cutoff(Å)	a(Å)	B_0(GPa)	Time (m)	a(Å)	B_0(GPa)	Time (m)
4.4	4.318	108.7	20.02	4.321	104.0	7.10
4.7	4.317	111.7	39.88	4.320	109.4	10.35
5.0	4.323	106.3	44.45	4.324	104.1	20.36
5.6	4.317	112.7	85.53	4.317	110.2	32.06
6.2	4.321	107.3	63.93	4.321	104.4	58.44
7.1	4.322	106.1	162.85	4.322	105.4	206.46

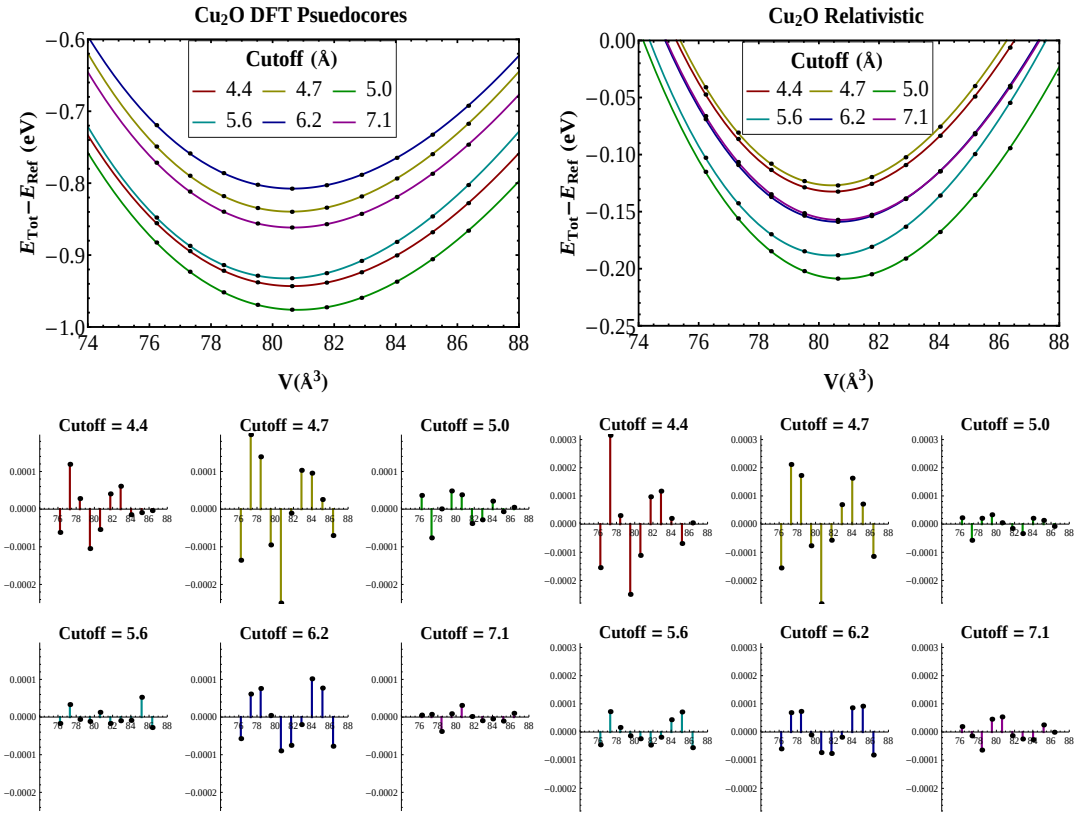

Figure A.2: Cu_2O total energy vs volume. The values of the total energy calculated with various orbital cutoff values have been fitted to Eq. A.1. The energy values plotted against the Y axis for the all-electron and pseudopotential cases are scaled by $E_{Ref} = -183497$ and $E_{Ref} = -28313$, respectively. The six smaller plots below each large plot show the residuals to each cutoff fit.

A.4 Conclusion

For the six cutoff values considered, the 5.0 Å cutoff yielded the lowest energy for in both copper and Cu_2O calculations using each of the three core treatments. According to the residual plots, the cutoff values of 4.4 and 4.7 Å showed the greatest error to the fit of the Murnaghan equation of state while the higher values showed much better fits. This is not surprising since, in reality, the electron wave functions extend to infinity, hence larger cutoffs should give more correct representation of the true wave functions leading to more accurate results.

Table A.3: Bulk properties of copper and Cu_2O. The minimized lattice constant a_0, nearest neighbor distances d_{Cu-Cu} and d_{O-O} and the Cu-O bond length d_{Cu-O} are all given in units of Å.

	Cu		Cu_2O			
	a_0	d_{Cu-Cu}	a_0	d_{Cu-Cu}	d_{O-O}	d_{Cu-O}
Present work	3.65	2.58	4.32	3.06	3.75	1.87
Experiment [97, 98]	3.61	2.55	4.27	3.02	3.68	1.84

In comparing these three methods we find that while the relativistic core treatment produces values closest to the experimental values, the DFT Psuedo-core values differ only slightly by ≈ 0.002 Å and cost about half as much in comparison. For this reason, pseudopotentials with relativistic effects will be used for all calculations performed in this thesis.

REFERENCES

[1] U. R. Evans. *The Corrosion and Oxidation of Metals*. Hodder Arnold, 1960.

[2] Yea-Yang Su and Robert M. Shemenski. The role of oxide structure on copper wire to the rubber adhesion. *Applied Surface Science*, 161(3-4):355 – 364, 2000.

[3] Kilwon Cho and Eun Chul Cho. Effect of the microstructure of copper oxide on the adhesion behavior of epoxy/copper leadframe joints. *Journal of Adhesion Science and Technology*, 14:1333–1353(21), 2000.

[4] Mohamed Lebbai, Jang-Kyo Kim, W. K. Szeto, Matthew M. F. Yuen, and Pin Tong. Optimization of black oxide coating thickness as an adhesion promoter for copper substrate in plastic integrated-circuit packages. *Journal of Electronic Materials*, 32(6):558–563, Jun 2003.

[5] Hai Bo Fan, Edward K. L. Chan, Cell K. Y. Wong, and Matthew M. F. Yuen. Molecular dynamics simulation of thermal cycling test in electronic packaging. *Journal of Electronic Packaging*, 129(1):35–40, 2007.

[6] Chun-Che Shih, Chun-Ming Shih, Yea-Yang Su, Lin Hui Julie Su, Mau-Song Chang, and Shing-Jong Lin. Quantitative evaluation of thrombosis by electrochemical methodology. *Thrombosis Research*, 111(1-2):103 – 109, 2003.

[7] Chun-Che Shih, Chun-Ming Shih, Yea-Yang Su, Rosario A. Gerhardt, and Shing-Jong Lin. The interaction of selected semiconducting biomaterials with platelet-rich plasma and whole blood. *Journal of Biomedical Materials Research Part A*, 74A(3):325–337, 2005.

[8] N. Mora, E. Cano, E. M. Mora, and J. M. Bastidas. Influence of ph and oxygen on copper corrosion in simulated uterine fluid. *Biomaterials*, 23(3):667 – 671, 2002.

[9] H. Over and A. P. Seitsonen. Oxidation of metal surfaces. *Science*, 297:2003, 2002.

[10] Gui-Chang Wang, Ling Jiang, Xian-Yong Pang, Zun-Sheng Cai, Yin-Ming Pan, Xue-Zhuang Zhao, Yoshitada Morikawa, and Junji Nakamura. A theoretical study of surface-structural sensitivity of the reverse water-gas shift reaction over cu(hkl) surfaces. *Surface Science*, 543(1-3):118 – 130, 2003.

[11] Ling Jiang, Gui-Chang Wang, Zun-Sheng Cai, Yin-Ming Pan, and Xue-Zhuang Zhao. Promotion of the water-gas shift reaction by pre-adsorbed oxygen on cu(hkl) surfaces: a theoretical study. *Journal of Molecular Structure: THEOCHEM*, 710(1-3):97 – 104, 2004.

[12] T. Mahalingam, J. S. P. Chitra, J. P. Chu, Hosun Moon, Han Joon Kwon, and Yong Deak Kim. Photoelectrochemical solar cell studies on electroplated cuprous oxide thin films. *Journal of Materials Science: Materials in Electronics*, 17(7):519–523, Jul 2006.

[13] Ki Hyun Yoon, Woo Jin Choi, and Dong Heon Kang. Photoelectrochemical properties of copper oxide thin films coated on an n-si substrate. *Thin Solid Films*, 372(1-2):250 – 256, 2000.

[14] Yatendra S. Chaudhary, Anshul Agrawal, Rohit Shrivastav, Vibha R. Satsangi, and Sahab Dass. A study on the photoelectrochemical properties of copper oxide thin films. *International Journal of Hydrogen Energy*, 29(2):131 – 134, 2004.

[15] Hans van't Spijker, Dan Simon, and Frans Ooms. Photocatalytic water splitting by means of undoped and doped la_2cuo_4 photocathodes. *International Journal of Hydrogen Energy*, 33(22):6414 – 6419, 2008.

[16] Sung Real Son, Kang Seok Go, and Sang Done Kim. Thermogravimetric analysis of copper oxide for chemical-looping hydrogen generation. *Industrial and Engineering Chemistry Research*, 48(1):380–387, 2009.

[17] D. Barreca, P. Fornasiero, A. Gasparotto, V. Gombac, C. Maccato, T. Montini, and E. Tondello. The potential of supported cu_2o and cuo nanosystems in photocatalytic h_2 production. *ChemSusChem*, 2(3):230–233, 2009.

[18] Valery M. Dubin. Electrochemical aspects of new materials and technologies in microelectronics. *Microelectronic Engineering*, 70(2-4):461 – 469, 2003. Materials for Advanced Metallization 2003.

[19] K. P. Rodach, T. Bohnen and K. M. Ho. First principles calculations of lattice relaxation at low index surfaces of cu. *Surface Science*, 286(1–2):66–72, 1993.

[20] Sergey Stolbov and Talat S. Rahman. Relationship between electronic and geometric structures of the o/cu(001) system. *The Journal of Chemical Physics*, 117(18):8523–8530, 2002.

[21] T. Lederer, D. Arvanitis, G. Comelli, L. Tröger, and K. Baberschke. Adsorption of oxygen on cu(100). i. local structure and dynamics for two atomic chemisorption states. *Phys. Rev. B*, 48(20):15390–15404, Nov 1993.

[22] T. Kangas, K. Laasonen, Puisto A., H. Pitknen, and Alatalo M. On-surface and sub-surface oxygen on ideal and reconstructed cu(100). *Surface Science*, 584(1):62 – 69, 2005. Selected papers of the Fifth Nordic Conference on Surface Science (NCSS-5).

[23] M. J. Harrison, D. P. Woodruff, J. Robinson, D. Sander, W. Pan, and J. Kirschner. Adsorbate-induced surface reconstruction and surface-stress changes in cu(100)/o: Experiment and theory. *Physical Review B (Condensed Matter and Materials Physics)*, 74(16):165402, 2006.

[24] M. Kittel, M. Polcik, R. Terborg, J. T. Hoeft, P. Baumgrtel, A. M. Bradshaw, R. L. Toomes, J. H. Kang, D. P. Woodruff, M. Pascal, C. L. A. Lamont, and E. Rotenberg. The structure of oxygen on cu(100) at low and high coverages. *Surface Science*, 470(3):311 – 324, 2001.

[25] Aloysius Soon, Mira Todorova, Bernard Delley, and Catherine Stampfl. Oxygen adsorption and stability of surface oxides on cu(111): A first-principles investigation. *Physical Review B (Condensed Matter and Materials Physics)*, 73(16):165424, 2006.

[26] M. Wuttig, R. Franchy, and H. Ibach. Oxygen on cu(100) - a case of an adsorbate induced reconstruction. *Surface Science*, 213(1):103 – 136, Jan 1989.

[27] Teija Kangas and Kari Laasonen. Dft study of reconstructed cu(1 0 0) surface with high oxygen coverages. *Surface Science*, 602(21):3239–3245, Nov 2008.

[28] Aloysius Soon, Mira Todorova, Bernard Delley, and Catherine Stampfl. Thermodynamic stability and structure of copper oxide surfaces: A first-principles investigation. *Physical Review B (Condensed Matter and Materials Physics)*, 75(12):125420, 2007.

[29] S. Jaatinen, J. Blomqvist, P. Salo, A. Puisto, M. Alatalo, M. Hirsimäki, M. Ahonen, and M. Valden. Adsorption and diffusion dynamics of atomic and molecular oxygen on reconstructed cu(100). *Physical Review B (Condensed Matter and Materials Physics)*, 75(7):075402, 2007.

[30] M. Lampimäki, K. Lahtonen, M. Hirsimäki, and M. Valden. Nanoscale oxidation of cu(100): Oxide morphology and surface reactivity. *The Journal of Chemical Physics*, 126(3):034703, 2007.

[31] I. Merrick, J. E. Inglesfield, and H. Ishida. Electronic structure and surface reconstruction of adsorbed oxygen on copper(001). *Surface Science*, 551(3):158 – 170, 2004.

[32] Sergey Stolbov, Abdelkader Kara, and Talat S. Rahman. Electronic structure of the $c(2 \times 2)o/cu(001)$ system. *Phys. Rev. B*, 66(24):245405, Dec 2002.

[33] P. Hohenberg and W. Kohn. Inhomogeneous electron gas. *Phys. Rev.*, 136(3B):B864–B871, Nov 1964.

[34] W. Kohn and L. J. Sham. Self-consistent equations including exchange and correlation effects. *Phys. Rev.*, 140(4A):A1133–A1138, Nov 1965.

[35] J. C. Slater. The theory of complex spectra. *Phys. Rev.*, 34(10):1293–1322, Nov 1929.

[36] John P. Perdew and Yue Wang. Accurate and simple analytic representation of the electron-gas correlation energy. *Phys. Rev. B*, 45(23):13244–13249, Jun 1992.

[37] Murray Gell-Mann and Keith A. Brueckner. Correlation energy of an electron gas at high density. *Phys. Rev.*, 106(2):364–368, Apr 1957.

[38] D. M. Ceperley and B. J. Alder. Ground state of the electron gas by a stochastic method. *Phys. Rev. Lett.*, 45(7):566–569, Aug 1980.

[39] J. P. Perdew, K. Burke, and M. Ernzerhof. Generalized gradient approximation made simple. *Phys. Rev. Lett.*, 77(18):3865–3868, Oct 1996.

[40] Yue Wang and John P. Perdew. Spin scaling of the electron-gas correlation energy in the high-density limit. *Phys. Rev. B*, 43(11):8911–8916, Apr 1991.

[41] J. C. Slater. The self consistent field and the structure of atoms. *Phys. Rev.*, 32(3):339–348, Sep 1928.

[42] J. C. Slater. Note on hartree's method. *Phys. Rev.*, 35(2):210–211, Jan 1930.

[43] V. Fock. Näherungs methode zur losung des quanten mechanischen mehrkörper probleme. *Zeitschrift für Physik A Hadrons and Nuclei*, 61(1–2):126–148, Jan 1930.

[44] John P. Perdew, Stefan Kurth, Ale š Zupan, and Peter Blaha. Accurate density functional with correct formal properties: A step beyond the generalized gradient approximation. *Phys. Rev. Lett.*, 82(12):2544–2547, Mar 1999.

[45] John P. Perdew, Jianmin Tao, Viktor N. Staroverov, and Gustavo E. Scuseria. Meta-generalized gradient approximation: Explanation of a realistic nonempirical density functional. *The Journal of Chemical Physics*, 120(15):6898–6911, 2004.

[46] Jorge Kohanoff. *Electronic structure calculations for solids and molecules: theory and computational methods*. Cambridge University Press, New York, 2006.

[47] B. Delley. An all-electron numerical method for solving the local density functional for polyatomic molecules. *The Journal of Chemical Physics*, 92(1):508–517, 1990.

[48] B. Delley. From molecules to solids with the dmol[sup 3] approach. *The Journal of Chemical Physics*, 113(18):7756–7764, 2000.

[49] Charles Kittel. *Introduction to solid state physics*. John Wiley and Sons, New York, 7 edition, 1996.

[50] Wei-Xue Li, Catherine Stampfl, and Matthias Scheffler. Oxygen adsorption on ag(111): A density-functional theory investigation. *Phys. Rev. B*, 65(7):075407, Jan 2002.

[51] Mira Todorova, Karsten Reuter, and Matthias Scheffler. Oxygen overlayers on pd(111) studied by density functional theory. *The Journal of Physical Chemistry B*, 108(38):14477–14483, 2004.

[52] M. V. Ganduglia-Pirovano and M. Scheffler. Structural and electronic properties of chemisorbed oxygen on rh(111). *Phys. Rev. B*, 59(23):15533–15543, Jun 1999.

[53] H. J. Monkhorst and J. D. Pack. Special points for brillouin-zone integrations. *Phys. Rev. B*, 13(12):5188–5192, Jun 1976.

[54] Juarez L. F. Da Silva, K. Schroeder, and S. Blügel. First-principles investigation of the multilayer relaxation of stepped cu surfaces. *Phys. Rev. B*, 69(24):245411, Jun 2004.

[55] H. L. Davis and J. R. Noonan. Cu(100) multilayer relaxation. *Journal of Vacuum Science and Technology*, 20(3):842–845, 1982.

[56] H.L. Davis and J.R. Noonan. Multilayer relaxation in metallic surfaces as demonstrated by leed analysis. *Surface Science*, 126(1-3):245 – 252, 1983.

[57] D. M. Lind, F. B. Dunning, G. K. Walters, and H. L. Davis. Surface-structural analysis by use of spin-polarized low-energy electron diffraction: An investigation of the cu(100) surface. *Phys. Rev. B*, 35(17):9037–9044, Jun 1987.

[58] Ch. Ross, B. Schirmer, M. Wuttig, Y. Gauthier, G. Bihlmayer, and S. Blügel. Structure, growth, and magnetism of mn on cu(110). *Phys. Rev. B*, 57(4):2607–2620, Jan 1998.

[59] D. L. Adams, H. B. Nielsen, J. N. Andersen, I. Stensgaard, R. Feidenhans'l, and J. E. Sørensen. Oscillatory relaxation of the cu(110) surface. *Phys. Rev. Lett.*, 49(9):669–672, Aug 1982.

[60] H.L. Davis, J.R. Noonan, and L.H. Jenkins. Determination of a cu(110) surface contraction by leed intensity analysis. *Surface Science*, 83(2):559 – 571, 1979.

[61] J.R. Noonan and H.L. Davis. Limitations in specular beam leed analysis due to measurement of the scattering angle: Examples from a study of cu(110). *Surface Science*, 99(3):L424 – L428, 1980.

[62] J. L. Da Silva. *The Nature and Behavior of Rare-Gas Atoms on Metal Surfaces.* PhD thesis, Technical University Berlin, July 2002.

[63] S. P. Tear, K. Roll, and M. Prutton. A comparison of reliability (r) factors in a leed structural analysis of the copper (111) surface. *Journal of Physics C Solid State Physics*, 14:3297–3311, aug 1981.

[64] S. Å. Lindgren, L. Walldén, J. Rundgren, and P. Westrin. Low-energy electron diffraction from cu(111): Subthreshold effect and energy-dependent inner potential; surface relaxation and metric distances between spectra. *Phys. Rev. B*, 29(2):576–588, Jan 1984.

[65] Ž. Crljen, P. Lazić, D. Šokčević, and R. Brako. Relaxation and reconstruction on (111) surfaces of au, pt, and cu. *Phys. Rev. B*, 68(19):195411, Nov 2003.

[66] R. Smoluchowski. Anisotropy of the electronic work function of metals. *Phys. Rev.*, 60(9):661–674, Nov 1941.

[67] P. O. Gartland, S. Berge, and B. J. Slagsvold. Photoelectric work function of a copper single crystal for the (100), (110), (111), and (112) faces. *Phys. Rev. Lett.*, 28(12):738–739, Mar 1972.

[68] H. M. Polatoglou, M. Methfessel, and M. Scheffler. Vacancy-formation energies at the (111) surface and in bulk al, cu, ag, and rh. *Phys. Rev. B*, 48(3):1877–1883, Jul 1993.

[69] T. Fauster and W. Steinmann. *Electromagnetic Waves: Recent Developments in Research*, volume 2, chapter 8, pages 347–411. Elsevier, Amsterdam, 1995.

[70] H. L. Skriver and N. M. Rosengaard. Surface energy and work function of elemental metals. *Phys. Rev. B*, 46(11):7157–7168, Sep 1992.

[71] G. A. Haas and R. E. Thomas. Work function and secondary emission studies of various cu crystal faces. *Journal of Applied Physics*, 48(1):86–93, 1977.

[72] T.A. Delchar. Oxygen chemisorption on copper single crystals. *Surface Science*, 27(1):11 – 20, 1971.

[73] J. L. F. Da Silva, C. Stampfl, and M. Scheffler. Converged properties of clean metal surfaces by all-electron first-principles calculations. *Surface Science*, 600(3):703 – 715, 2006.

[74] H. Bross and M. Kauzmann. Electronic structure, surface states, surface energy, and work function of the cu(100) surface. *Phys. Rev. B*, 51(23):17135–17150, Jun 1995.

[75] Gary G. Tibbetts, James M. Burkstrand, and J. Charles Tracy. Electronic properties of adsorbed layers of nitrogen, oxygen, and sulfur on copper (100). *Phys. Rev. B*, 15(8):3652–3660, Apr 1977.

[76] P. O. Gartland and B. J. Slagsvold. Transitions conserving parallel momentum in photoemission from the (111) face of copper. *Phys. Rev. B*, 12(10):4047–4058, Nov 1975.

[77] D. E. Eastman and J. K. Cashion. Photoemission from cu, ag, and au in the 10- to 27-ev energy range. *Phys. Rev. Lett.*, 24(7):310–313, Feb 1970.

[78] J. G. Gay, J. R. Smith, and F. J. Arlinghaus. Large surface-state/surface-resonance density on copper (100). *Phys. Rev. Lett.*, 42(5):332–335, Jan 1979.

[79] U. Döbler, K. Baberschke, J. Stöhr, and D. A. Outka. Structure of c(2times2) oxygen on cu(100): A surface extended x-ray absorption fine-structure study. *Phys. Rev. B*, 31(4):2532–2534, Feb 1985.

[80] Takaya Fujita, Yuji Okawa, Yuji Matsumoto, and Ken-ichi Tanaka. Phase boundaries of nanometer scale c(2times2)-o domains on the cu(100) surface. *Phys. Rev. B*, 54(3):2167–2174, Jul 1996.

[81] K. W. Jacobsen and J. K. No?rskov. Theory of the oxygen-induced restructuring of cu(110) and cu(100) surfaces. *Phys. Rev. Lett.*, 65(14):1788–1791, Oct 1990.

[82] J. G. Tobin, L. E. Klebanoff, D. H. Rosenblatt, R. F. Davis, E. Umbach, A. G. Baca, D. A. Shirley, Y. Huang, W. M. Kang, and S. Y. Tong. Normal photoelectron diffraction of o/cu(001): A surface-structural determination. *Phys. Rev. B*, 26(12):7076–7078, Dec 1982.

[83] T. Wiell, J. E. Klepeis, P. Bennich, O. Björneholm, N. Wassdahl, and A. Nilsson. Local aspects of the adsorbate-substrate chemical bond in n/cu(100) and o/cu(100). *Phys. Rev. B*, 58(3):1655–1664, Jul 1998.

[84] R. Mayer, Chun-Si Zhang, and K. G. Lynn. Evidence for the absence of a $c(2\times2)$ superstructure for oxygen on cu(100). *Phys. Rev. B*, 33(12):8899–8902, Jun 1986.

[85] I. K. Robinson, E. Vlieg, and S. Ferrer. Oxygen-induced missing-row reconstruction of cu(001) and cu(001)-vicinal surfaces. *Phys. Rev. B*, 42(11):6954–6962, Oct 1990.

[86] F. Jensen, F. Besenbacher, E. Laegsgaard, and I. Stensgaard. Dynamics of oxygen-induced reconstruction of cu(100) studied by scanning tunneling microscopy. *Phys. Rev. B*, 42(14):9206–9209, Nov 1990.

[87] M.C. Asensio, M.J. Ashwin, A.L.D. Kilcoyne, D.P. Woodruff, A.W. Robinson, Th. Lindner, J.S. Somers, D.E. Ricken, and A.M. Bradshaw. The structure of oxygen adsorption phases on cu(100). *Surface Science*, 236(1-2):1 – 14, 1990.

[88] H.C. Zeng and K.A.R. Mitchell. Further leed investigations of missing row models for the surface structure. *Surface Science*, 239(3):L571 – L578, 1990.

[89] E. A. Colbourn and J. E. Inglesfield. Effective charges and the surface stability of o on cu(001). *Phys. Rev. Lett.*, 66(15):2006–2009, Apr 1991.

[90] P. Hofmann, R. Unwin, W. Wyrobisch, and A.M. Bradshaw. The adsorption and incorporation of oxygen on cu(100) at t [greater-or-equal, slanted] 300 k. *Surface Science*, 72(4):635 – 644, 1978.

[91] Accelrys Software Inc. *Materials Studio Release Notes*. Accelrys Software Inc., San Diego, 44 edition, 2008.

[92] D D Koelling and B N Harmon. A technique for relativistic spin-polarised calculations. *Journal of Physics C: Solid State Physics*, 10(16):3107–3114, 1977.

[93] M. Douglas and N. M. Kroll. Quantum electrodynamical corrections to the fine structure of helium. *Annals of Physics*, 82(1):89–155, 1974.

[94] B. Delley. Hardness conserving semilocal pseudopotentials. *Phys. Rev. B*, 66(15):155125, Oct 2002.

[95] Aloysius Soon, Xiang-Yuan Cui, Bernard Delley, Su-Huai Wei, and Catherine Stampfl. Native defect-induced multifarious magnetism in nonstoichiometric cuprous oxide: First-principles study of bulk and surface properties of cu[sub 2 - delta]o. *Physical Review B (Condensed Matter and Materials Physics)*, 79(3):035205, 2009.

[96] F. D. Murnaghan. The compressibility of media under extreme pressures. *Proceedings of the National Academy of Sciences of the United States of America*, 30(9):244–247, Sep 1944.

[97] N. W. Ashcroft and N. D. Mermin. *Solid State Physics*. Holt, Rienhart, and Winston, New York, 1976.

[98] A. Werner and H. D. Hochheimer. High-pressure x-ray study of *cu*2o and *ag*2o. *Phys. Rev. B*, 25(9):5929–5934, May 1982.

BIOGRAPHICAL STATEMENT

Willie Burton Maddox IV was born in Key West Florida in 1976. He graduated high school in 1995. From 1998 to 2002 he served in the United States Navy as an Aviation Electronics Technitian for Electronic Attack Squadron one-three-two. He received his B.S. degree from the University of Alabama in Huntsville in 2006 with a focus on space plasma physics and his M.S. degree in 2008 from The University of Texas at Arlington in the field of condensed mater physics. He is a member of several scientific and academic societies. He enjoys disk golf, racquetball and playing guitar.